REPORT DOCUMENTATION PAGE

Form Approved OMB NO. 0704-0188

1. REPORT DATE (DD-MM-YYYY)	2. REPORT TYPE	3. DATES COVERED (From - To)
16-01-2015	Final Report	17-Oct-2011 - 16-Oct-2014

4. TITLE AND SUBTITLE

Final Report: Fundamental Investigation of Jet Fuel Spray and Ignition Process in an Optically Accessible Piston Engine

5a. CONTRACT NUMBER
W911NF-11-1-0533

5b. GRANT NUMBER

5c. PROGRAM ELEMENT NUMBER
611102

6. AUTHORS

Nicholas Neal, David Rothamer

5d. PROJECT NUMBER

5e. TASK NUMBER

5f. WORK UNIT NUMBER

7. PERFORMING ORGANIZATION NAMES AND ADDRESSES

University of Wisconsin - Madison
21 NORTH PARK STREET SUITE 6401

MADISON, WI 53715 -1218

8. PERFORMING ORGANIZATION REPORT NUMBER

9. SPONSORING/MONITORING AGENCY NAME(S) AND ADDRESS (ES)

U.S. Army Research Office
P.O. Box 12211
Research Triangle Park, NC 27709-2211

10. SPONSOR/MONITOR'S ACRONYM(S)
ARO

11. SPONSOR/MONITOR'S REPORT NUMBER(S)
60579-EG.2

12. DISTRIBUTION AVAILIBILITY STATEMENT

Approved for Public Release; Distribution Unlimited

13. SUPPLEMENTARY NOTES

The views, opinions and/or findings contained in this report are those of the author(s) and should not contrued as an official Department of the Army position, policy or decision, unless so designated by other documentation.

14. ABSTRACT

Effects of transient rate-of-injection (ROI) fuel sprays on jet development and combustion were measured in a compression-ignition direct-injection optical engine. Jet penetration, liquid length, jet dispersion angle, liftoff length, and engine cylinder pressure data were simultaneously acquired over a range of engine operating conditions relevant to the design of Army engines. Tests were performed using #2 diesel fuel, jet fuel (JP8), and a hydroprocessed renewable jet fuel (HRJ). Ambient thermodynamic conditions and fuel injection parameters had similar effects on combustion and jet performance in the optical engine as in previous results from constant volume

15. SUBJECT TERMS

Transient, diesel, injection, optical engine

16. SECURITY CLASSIFICATION OF:			17. LIMITATION OF ABSTRACT	15. NUMBER OF PAGES	19a. NAME OF RESPONSIBLE PERSON
a. REPORT	b. ABSTRACT	c. THIS PAGE			David Rothamer
UU	UU	UU	UU		19b. TELEPHONE NUMBER 608-890-2271

Report Title

Final Report: Fundamental Investigation of Jet Fuel Spray and Ignition Process in an Optically Accessible Piston Engine

ABSTRACT

Effects of transient rate-of-injection (ROI) fuel sprays on jet development and combustion were measured in a compression-ignition direct-injection optical engine. Jet penetration, liquid length, jet dispersion angle, liftoff length, and engine cylinder pressure data were simultaneously acquired over a range of engine operating conditions relevant to the design of Army engines. Tests were performed using #2 diesel fuel, jet fuel (JP8), and a hydroprocessed renewable jet fuel (HRJ). Ambient thermodynamic conditions and fuel injection parameters had similar effects on combustion and jet performance in the optical engine as in previous results from constant volume chambers. The ramp-on transient from the opening of the fuel injector caused the scaling of jet parameters with time during the transient ROI to be modified from relationships expected from the literature. Similarities were seen in a comparison between the jet velocity, the derivative of the ROI and the derivative of a curve fit created to model the data taken. In the long-time limit, these injections were seen to return to their quasi-steady forms, with the changes in jet parameters occurring during the initial opening of the injector. The results show the need to resolve the initial transient injection process in small bore diesel engines.

Enter List of papers submitted or published that acknowledge ARO support from the start of the project to the date of this printing. List the papers, including journal references, in the following categories:

(a) Papers published in peer-reviewed journals (N/A for none)

Received		Paper
04/18/2013	1.00	Nicholas James Neal, Jonny Jordan, David Rothamer. Simultaneous Measurements of In-Cylinder Temperature and Velocity Distribution in a Small-Bore Diesel Engine Using Thermographic Phosphors, SAE International Jounal of Engines, (05 2013): 0. doi:
TOTAL:	**1**	

Number of Papers published in peer-reviewed journals:

(b) Papers published in non-peer-reviewed journals (N/A for none)

Received		Paper
TOTAL:		

Number of Papers published in non peer-reviewed journals:

(c) Presentations

Number of Presentations: 0.00

Non Peer-Reviewed Conference Proceeding publications (other than abstracts):

Received Paper

TOTAL:

Number of Non Peer-Reviewed Conference Proceeding publications (other than abstracts):

Peer-Reviewed Conference Proceeding publications (other than abstracts):

Received Paper

TOTAL:

Number of Peer-Reviewed Conference Proceeding publications (other than abstracts):

(d) Manuscripts

Received Paper

TOTAL:

Number of Manuscripts:

Books

Received Book

TOTAL:

Received Book Chapter

TOTAL:

Patents Submitted

Patents Awarded

Awards

Graduate Students

NAME	PERCENT_SUPPORTED	Discipline
Nicholas Neal	1.00	
FTE Equivalent:	**1.00**	
Total Number:	**1**	

Names of Post Doctorates

NAME	PERCENT_SUPPORTED
FTE Equivalent:	
Total Number:	

Names of Faculty Supported

NAME	PERCENT_SUPPORTED	National Academy Member
David Rothamer	0.08	No
FTE Equivalent:	**0.08**	
Total Number:	**1**	

Names of Under Graduate students supported

NAME	PERCENT_SUPPORTED
FTE Equivalent:	
Total Number:	

Student Metrics

This section only applies to graduating undergraduates supported by this agreement in this reporting period

The number of undergraduates funded by this agreement who graduated during this period: 0.00

The number of undergraduates funded by this agreement who graduated during this period with a degree in science, mathematics, engineering, or technology fields:..... 0.00

The number of undergraduates funded by your agreement who graduated during this period and will continue to pursue a graduate or Ph.D. degree in science, mathematics, engineering, or technology fields:..... 0.00

Number of graduating undergraduates who achieved a 3.5 GPA to 4.0 (4.0 max scale):..... 0.00

Number of graduating undergraduates funded by a DoD funded Center of Excellence grant for Education, Research and Engineering:..... 0.00

The number of undergraduates funded by your agreement who graduated during this period and intend to work for the Department of Defense 0.00

The number of undergraduates funded by your agreement who graduated during this period and will receive scholarships or fellowships for further studies in science, mathematics, engineering or technology fields: 0.00

Names of Personnel receiving masters degrees

NAME
Total Number:

Names of personnel receiving PHDs

NAME
Total Number:

Names of other research staff

NAME	PERCENT_SUPPORTED
FTE Equivalent:	
Total Number:	

Sub Contractors (DD882)

Inventions (DD882)

Scientific Progress

See Attachment

Technology Transfer

Final Report: Fundamental Investigation of Jet Fuel Spray and Ignition Process in an Optically Accessible Piston Engine

DOCUMENT: ARO Final Report
PRINCIPAL INVESTIGATOR: David Rothamer
GRADUATE STUDENT: Nicholas Neal
January 16, 2015

Contents

Abstract

Effects of transient rate-of-injection (ROI) on jet development and combustion were measured in a compression-ignition direct-injection optical engine. Jet penetration, liquid length, jet dispersion angle, liftoff length, and engine cylinder pressure data were simultaneously acquired over a range of engine operating conditions relevant to the design of Army engines. Tests were performed using #2 diesel fuel, jet fuel (JP8), and a hydroprocessed renewable jet fuel (HRJ). Ambient thermodynamic conditions and fuel injection parameters had similar effects on combustion and jet performance in the optical engine as in previous results from constant volume chambers. The higher volatility and lower density of the jet fuels relative to #2 diesel fuel resulted in shorter liquid lengths for the jet fuels and slight differences in the jet dispersion and penetration. However, the lift-off length and ignition delay for the JP8 fuel were almost identical to the #2 diesel fuel with matched cetane number, indicating that cetane number has a stronger influence than changes in fuel physical properties on the combustion process. The ramp-on transient from the opening of the fuel injector caused the scaling of jet parameters with time during the transient ROI to be modified from relationships expected from the literature for all of the fuels. Initial penetration of the jets was proportional to t^a where a is had values significantly > 1 (typically in the range of 1.5 to 2.0 dependent upon injection pressure) at the SOI and shortly after in comparison to the t^1 scaling with time often assumed in the literature. Similarities were seen in a comparison between the jet velocity and the derivative of the fuel mass ROI. In the long-time limit, injections were seen to return to their quasi-steady forms once fuel mass ROI had become approximately steady, with the changes in jet parameters occurring during the initial opening of the injector. The differences observed in jet penetration during the injector ramp-on transient will effect the overall jet penetration and ignition delay and liftoff length and are important to model, especially for injections with short overall duration or long injector transient where the transient period encompasses a significant fraction of the injection process.

1 Introduction and Motivation

The compression ignition (CI) internal combustion engine has been one of the primary power plants of the past 100 years due to its high efficiency and power-to-weight ratio [1]. Most modern versions use a fuel delivery system composed of a high-pressure injector mounted to inject fuel directly into the combustion chamber, a process known as direct injection (DI). During injection, fuel is vaporized by and mixed with the dense hot in-cylinder gases leading to autoignition of the spray. This process is central to the performance of the engine [2]. The start-of-combustion is preceded by a combination of physical and chemical processes, encompassing: the fluid dynamics of fuel-oxidizer mixing, the thermodynamics of ambient and local conditions in the spray, and the reaction pathways that ultimately determine the mechanisms of ignition [3]. Under transient injection conditions, particularly relevant to small diesel engines of Army interest, the processes leading to ignition and combustion are directly impacted by the time-varying rate of fuel injection. The current work has focused on improving the understanding of the transient period of the injection process and the influence it has on the macroscopic behavior of the fuel jet up until ignition.

Vaporizing fuel jets have long been the subject of focused study in the field of internal combustion engines. The primary foci of previous research on this topic includes: the processes governing jet and spray penetration rates and distances, flame liftoff lengths, and ignition location and delay. The modern interpretation of the lifted diffusion flame in direct-injection diesel engines described by Dec [4] in 1997, and updated by Pickett and Siebers [5], involves a complex coupling of turbulent fluid mechanics with chemical reactions and combustion, that remains difficult to predict through analytical and computational means. Optical experimental techniques have been used extensively to provide a non-intrusive means for both gaining a physical understanding of these processes and for providing quantitative data against which computational models can be vetted or tuned. A recent paper by Som et al. [6] compared the predictive capabilities of current state-of-the-art commercial CFD software packages with respect to sprays and combustion, with the results of experimental data taken in a constant volume chamber [7]. The performance of the simulations was evaluated by their ability to predict jet characteristics such as vapor and liquid penetration of fuel jets, and combustion parameters including ignition and flame stabilization. While the CFD codes tested were able to predict jet and combustion behavior during quasi-steady operation relatively well, differences during transient periods were significant [6, 7]. An upper limit to the accuracy of CFD modeling of fuel jets is coupled to the accuracy of the rate-of-injection profile used for the fuel boundary condition [8].

The bulk of the research published to date has focused on the quasi-steady period of the injection process. While these results are useful for gaining a fundamental understanding of the combustion and mixing processes inherent in compression-ignition engines, they are not entirely representative of the actual conditions seen in real applications, especially in the case of the small-bore diesel engine. This type of engine often utilizes short injection durations (resulting in ramped rate-of-injection profiles) that do not correspond to the conditions under which many of the scaling theories and dependencies set forth in the literature were developed. Additionally, engines operating with multi-

ple in-cylinder injections per cycle will similarly have injections dominated by ramped rate-of-injection profiles. Therefore, there is a strong need to gain an understanding of transient effects on jet development and combustion.

The completed work addresses this need through a fundamental optical study of transient rate-of-injection events in an optically accessible internal combustion engine. Measurements of fuel jet macroscopic behavior were performed using high-speed imaging of the in-cylinder fuel injection event to simultaneously measure liquid penetration, vaporized fuel penetration, jet spreading angle, and the liftoff length. Fuels used for the measurements included #2 diesel fuel, JP-8, and a hydroprocessed renewable jet fuel (HRJ). A smaller subset of measurements were performed with 50/50 blends (by volume) of isoparaffinic kerosene (IPK) and JP-8, and HRJ and JP-8. In-cylinder thermodynamic conditions were varied at the start-of-injection by varying the intake pressure and intake temperature to the engine. Three different injection pressures were utilized which provide three different rate-of-injection ramp profiles. The results provide measurements over a wide range of conditions relevant to the design of Army engines.

2 Scientific Background

The work presented in this report focuses on the development of transient fuel jets in diesel engines and the coupling between the transient jet and the combustion event. The following literature review provides an overview of previous work relevant to the completed project. First, an overview is given of the significant literature related to current understanding of both quasi-steady jets and recent work on transient jets, focusing on liquid and vapor penetration behavior and jet dispersion. This is followed by a discussion of aspects of the combustion process: jet ignition, flame stabilization, and the quasi-steady liftoff length. Finally, optical techniques and experimental facilities are reviewed.

The nomenclature used to describe the liquid and vapor portions of the injected fuel follows that of Pickett et al. [5], where the portion of the injection with liquid droplets present is referred to as the "spray," and the overall injection process involving the spray as well as the region composed of only fuel vapor and entrained ambient air is referred to as the "jet."

2.1 Quasi-Steady and Transient Jet Behavior

Analysis of diesel jets was already underway by the 1920s [9], although the majority of the work before the comprehensive study in 1996 by Naber and Siebers at Sandia National Labs [10] was performed under non-vaporizing (i.e. room temperature) conditions, focusing on the development of experimental correlations for jet penetration as a function of ambient gas density. Barring a few notable exceptions [11, 12], experimental conditions for these analyses were outside those seen in internal combustion engines. Also, much of the literature upon which current understanding of macroscopic jet behavior was developed focuses on the study of jets emitted from injection systems capable of "top-hat" injection profiles. These systems display turn-on times (time for the injector needle to fully open and reach a maximum fuel flow rate) on the order of 50 μs or less. The goal of these

studies in general was to study the quasi-steady portion of the injection process where the rate-of-injection is approximately constant, and the injector transient is generally ignored.

2.1.1 Dispersion Angle

The dispersion angle of a diesel fuel jet is related to its penetration characteristics through its ambient air entrainment rate. A larger spray spreading angle indicates that surrounding gases are more quickly entrained, allowing for faster vaporization and reduction in the total penetration distance. The dispersion measurements performed by Naber and Siebers [10] displayed local spray angles that remained fairly constant along the axis of the jet during the quasi-steady (developed) portion of the injection. Based on simple jet theory for a quasi-steady jet, the ambient gas entrainment rate is constant along the spray axis and proportional to three key variables: injector orifice diameter ($d_\circ$), fuel injection velocity (U_f, directly proportional to the square root of injection/ambient pressure difference), and the tangent of half the dispersion angle $tan(\theta/2)$. During the beginning and end of the injection events, an initial transient period was noted by Naber and Siebers where the dispersion angle was significantly larger than the quasi-steady value, an effect the authors hypothesized was due to needle movement in the injector but was not investigated further.

The dispersion angle has been shown to be independent of injection pressure in the quasi-steady regime in both vaporizing and non-vaporizing cases [10]. The spreading angle has been shown by multiple researchers under non-vaporizing cases to scale with the ratio of the ambient gas density to the fuel density (ρ_a/ρ_f) raised to a power, determined empirically [10, 11, 12, 13, 14]. The wide range of reported has been attributed to the sensitivity of the experimental measurement of the angle to experimental setup and image analysis [15, 5]. Under vaporizing conditions an overall decrease in spray dispersion angles was observed, although the effect decreased with increasing ambient pressure. This contraction is thought to be due to evaporative cooling of the entrained ambient gases.

Research studying the effect of acceleration on unsteady turbulent single-phase jets (notably [16, 17]) has shown that accelerating jets display decreased dispersion angles and entrainment rates, and vice versa for decelerating jets. The change in entrainment rates was attributed to the modified entrainment appetite of the flow, due to the difference in velocities of coherent structures along the axial direction of the jet [17]. This reduction in entrainment was modeled by Breidenthal [18], who developed a self-similar solution for a round exponentially accelerating jet, and concluded that the entrainment rate appetite of the large scale eddies is inhibited if they are followed by upstream neighboring structures of greater momentum. Other CFD studies were carried out corroborating these findings, including the unsteady Reynolds averaged Navier-Stokes simulations of Abani and Reitz [19] and direct numerical simulations (DNS) by Silva et al. [20]. The dispersion angle was measured during the accelerating portion of a non-vaporizing jet by Payri et. al. [21], where the angle decreased from its original value until the jet reached a quasi-steady state, similar to the results seen from Naber and Siebers [10]. Little to no experimental data on this parameter currently exists for transient jets under diesel engine-like conditions.

2.1.2 Jet Penetration

The propagation of the head of the fuel jet during the injection process is defined as the jet penetration. Naber and Siebers **[?]** were able to collapse all of their spray penetration data for all conditions using non-dimensional time and distance parameters derived from a simple jet model based on the earlier work of Wakuri et al. [22]. The jet model assumes a uniform steady velocity profile at any downstream position x, and a constant dispersion angle α. A no-slip condition was assumed between the fuel in the spray and the entrained air, and it was also assumed that the injection velocity was constant and neglects the initial turn-on transient. The analysis is technically only valid for incompressible and isothermal jets, although the authors successfully applied it to two-phase jets under vaporizing conditions as well.

Naber and Siebers ignored the initial rate-of-injection (ROI) ramp-up portion by extrapolating the "steady" ROI portion of the curve to zero penetration and defining that point as time zero. Defining t=0 in this way gave better conformation of the experimental data to the model, although it removes the ability of the model to predict the effect of initial transients. The final penetration correlation is provided in Equations 1 and 2 in the short and long time limits, respectively:

$$S = C_v \sqrt{2\frac{\Delta P}{\rho_f} t} \tag{1}$$

$$S = \sqrt{\frac{C_v * \sqrt{2 \cdot C_a}}{a \cdot \tan\theta/2}} \cdot \left(\frac{\Delta P}{\rho_a}\right)^{1/4} \cdot \sqrt{d_\circ \cdot t}, \tag{2}$$

where S is the penetration distance of the jet, dependent on the nozzle velocity and area coefficients C_v and C_a, pressure drop across the orifice ΔP, ambient and fuel densities ρ_a and ρ_f, constant a, orifice diameter d_o, and time t. These correlations show the same dependencies on pressure drop and time as previous work by Hiroyasu and Arai [11], Dent [23], and others. Also, the long-time scaling dependencies are the same as those seen for steady-state turbulent gas jets [24]. Naber and Siebers also noted that when substituting typical orifice parameters into their correlation, the initial scaling factor is also similar to previous work (2.95 for Hiroyasu and Arai, 3.07 for Dent, and 2.9 for Naber and Siebers) [10]. The transition period between these short and long-time behaviors is referred to in Hiroyasu and Arai as the spray breakup time, given in Equation 3,

$$t_{break} = 28.65 \frac{\rho_f d}{\sqrt{\rho_a \Delta_P}}, \tag{3}$$

and occurs as the jet shifts from being dominated by the liquid to the entrained gas.

These correlations identify a linear dependence of penetration on time for short times and a square root dependence for long times. Recent work [8] suggests, however, that the simple assumption of linear penetration at injector turn on is not necessarily a good one and that the behavior may be more complex even for injectors with near top-hat profiles. Top-hat injection profiles assume that the liquid spray velocity at the orifice is

immediately at its maximum value as soon as the injection event occurs, negating the initial ramp-up period.

Relatively little data have been gathered on vaporizing transient jets under diesel engine conditions. The scaling of spray penetration for non-vaporizing jets during the opening of the injector was studied by Kostas et al. [25] for ambient pressures up to 5 MPa using a single-hole common-rail diesel injector with high-speed imaging. The authors found that for the initial period during the opening of the injector, the injection velocity appeared to scale with time as $U \propto \sqrt{t}$, while the penetration distance scaled with time as $S \propto t^{3/2}$. Recent work by Pickett et al. [8] has provided initial insight into the effect of transient rate-of-injection on overall jet development. Analysis of mass- and momentum-based ROI data revealed that the initial transient opening time depends on the total flow area in the injector and that significant fluctuations in the ROI occur even after the injector appears to have fully opened.

Efforts have been made to model transient jet behavior with a limited computational cost using one-dimensional models of non-reacting, non-vaporizing jets [26, 27]. This model was recently updated by Pickett et. al. [5] to allow for variable dispersion angles. Employing the experimental ROI for the specific injector used in the measurements and allowing for a variable jet spreading angle greatly enables close matching of experimental data [5].

2.1.3 Liquid Length

The liquid length of a jet refers to the distance from the injector orifice to the point where liquid droplets are no longer detectable. Under high-temperature vaporizing conditions, such as those found in internal combustion engines, the jet begins as a spray where liquid penetration is equal to the overall jet penetration. As hot ambient gases are mixed into the spray, a point in the jet is reached where sufficient energy for all droplets to evaporate is entrained and the liquid phase completely disappears. Further penetration at this point is entirely vapor, and the liquid length fluctuates due to turbulence about a quasi-steady position, if ambient conditions remain constant [28].

The effects of ambient temperature and density on the liquid length of vaporizing jets were explored by Espey and Dec [29]. Higher temperatures provide more thermal energy for vaporization, decreasing liquid length and reducing chemical timescales for ignition. Higher in-cylinder densities increase ambient air entrainment into the jet. This leads to an entrainment-induced increase in the vaporization rate.

Liquid lengths decrease linearly with injector orifice diameter, approaching zero as orifice diameter is decreased towards zero [30, 28]. A fuel jet's liquid length is essentially independent of injection pressure[10, 31] since the increased rate of injected fuel mass is balanced by a corresponding increase ambient gase entrainment rate. The vaporization of fuel sprays under diesel engine conditions are dominated by entrainment through turbulent mixing, rather than "local interphase transport mechanics" [28]. This does not mean that these other processes are not important, only that they are not rate-limiting under typical diesel engine injection conditions.

Liquid length is non-linearly dependent on ambient density and temperature. It also is affected by fuel properties, namely fuel volatility. The effects of fuel type on liquid

length have been documented in multiple works, including [28, 32, 33]. Higgins [33] also developed an engineering correlation from empirical data to predict liquid length for a wide range of fuels, given a set of fuel properties. These correlations are based on results from quasi-steady injection measurements.

Fisher and Mueller [34, 35, 36] recently examined effects of transient conditions on fuel sprays in an optical engine. The experimental results (with the start of injection taken over a range of engine timings) matched those from Sieber's mixing limited vaporization model [30], as long as the instantaneous thermodynamic condition were used in the model. Increased temperature due to combustion heat release reduced the mean liquid length.

2.2 Liftoff Length and Ignition

The mixing and vaporization processes that dominate the formation of jets as described in the previous section also serve as determining factors for ignition and flame stabilization in the engine. The conceptual diesel jet combustion model, as developed by Dec et al. [4, 37] and more recently updated by Pickett and Siebers [38], describes the processes for mixing-controlled diesel combustion where a rich partially-premixed air-fuel mixture begins to combust at a downstream distance referred to as the liftoff length, creating a rich high-temperature region (suitable for soot formation) surrounded by a turbulent non-premixed flame. After the initial autoignition of the fuel jet, a quasi-steady liftoff length is established that is influenced by changes in the in-cylinder conditions. The exact physics behind the establishment of this location are still not fully known, and the focus of much of the work performed on combusting jets has been devoted to discerning whether this is an ignition-based or flame-propagation-driven process.

In hydrocarbon-oxygen chemical reactions, significant OH chemiluminescence occurs during high-temperature, near-stoichiometric combustion [39], and the beginning of this region marks the liftoff length of the flame [40]. This emission comes from the excited hydroxyl radical, OH*, formed during the exothermic reaction [39]:

$$CH + O_2 \rightarrow CO + OH^*. \tag{4}$$

The radical quickly returns to its ground state through a combination of collisional quenching and emission of chemiluminescence, the strongest band of which lies in a narrow region around 310 nm [39].

Siebers and Higgins [41] used emision from OH* to measure quasi-steady liftoff lengths in a CVC over a large range of ambient thermodynamic and injection conditions inclusive of those seen in modern diesel engines and determined power-law dependencies for liftoff on each parameter. The scaling relations were used to develop a power law correlation [42]:

$$H = C {T_a}^{-3.74} {\rho_a}^{-0.85} {d_\circ}^{0.34} U^1 {Z_{st}}^{-1} \tag{5}$$

where H [mm] is the liftoff length, C is a proportionality constant, T_a [K] is the ambient gas temperature, ρ_a [kg/m^3] is the ambient gas density, $d_\circ$ [mm] is the injector orifice diameter, U [m/s] is the fuel injection velocity at the orifice, and Z_{st} is the stoichiometric

mixture fraction. Liftoff length exhibits a strong non-linear dependence on thermodynamic conditions, an effect that the authors postulated is due in part to their influence on the laminar flame speed and thermal diffusivity. Also, unlike liquid length, the liftoff length is linearly dependent upon injection velocity, a behavior seen in combusting gas jets [40].

Fuel autoignition chemistry also directly effects the liftoff length. Fuels with the longer ignition delays generally show longer liftoff lengths [42]. This potentially indicates that ignition is indeed a factor in the stabilization of the lifted flame. However, there are cases where the liftoff length ordering does not follow ordering based on ignition delay, indicating that the correlation between ignition delay and liftoff length is not always one-to-one [42]. Additional liftoff fuels studies include [43, 44, 45].

It is specifically mentioned by Pickett et al. [46] that the correlation given in Equation 5 likely would not hold for transient jets, due to the coupling of the spatial location of the initial flame kernels with the established quasi-steady location. CFD simulations were performed by Juneja et al. [47] exploring the effect of the injection rate-shape on diesel combustion where jets with top-hat, accelerating, and decelerating ROIs were tested. The modeling was performed using detailed chemistry in a simulated CVC that was able to produce lifted-flame behavior. The top-hat ROI profile simulations agreed with the results from Pickett et al. [42], but significant differences were seen in the cases with accelerating and decelerating ROI profiles. For the decelerating rate shape, the liftoff length was shown to decrease over time, an expected result as the injection velocity was decreasing. However, for the accelerating case, the initial liftoff length was short due to the initial low injection velocity and was maintained at this short length over the entire injection (a 4 ms event). It was postulated by the authors that this was due to hot combustion gases being built up around the initial ignition zone that then continued to convect into the mixing jet, such that even as the injection velocity increased by a factor of two, the liftoff length did not change appreciably. Regardless of the reasons, it was evident that transients in the ROI altered the liftoff length from its normal quasi-steady value.

2.3 Optics and Image Analysis

The following section provides a brief review of optical techniques relevant to sprays and combusting jets, focused predominantly on techniques that provide path integrated measurements that can be performed at very high repetition rates (limited mainly by camera technology) allowing for the temporal dynamics of diesel jets to be resolved. These techniques include schlieren and shadowgraphy for vapor measurements, Mie scattering for liquid penetration measurements, and chemiluminescence for liftoff length measurement.

Schlieren and shadowgraph techniques rely upon the change in refractive index associated with density gradients in a gases to bend light resulting in light and dark regions in an image [48]. A linear relationship exists between the density of a gas and its refractive index, given by:

$$n - 1 = k\rho \tag{6}$$

where n is the refractive index of the gas, k is the Gladstone-Dale constant, and ρ is the density of the gas.

In shadowgraphy, light from a source is refracted as it moves through a gas with a density gradient. Without the "shadowgraphy object" S in the way of the light source, the screen would be uniformly lit, but the gradients in the gas cause shadows to be cast in the far field, produced as the direction of the rays are modified by the test region [48]. In a simple schlieren setup, a collimated light source is passed through a test region and the light is refocused through a knife edge before being imaged onto a surface. The knife edge blocks light rays that were refracted by the density gradients, causing the re-expanded image to have dark regions where density gradients exist in the gas [48].

Chemiluminescence and incandescence that occur as a byproduct of combustion without external laser excitation are also useful sources for optical imaging. Chemiluminescence is radiation emitted from an excited species formed in a chemical reaction [49], while incandescence is thermal radiation from heated particles. Chemiluminescence for a specific transition of a specific species occurs in a specified wavelength band, and can therefore be targeted and imaged using a bandpass filter on the camera system. Incandescence on the other hand is broadband, exhibiting a Planck distribution as modified by the spectral emissivity of the emitting substance.

3 Experimental Method

The primary experimental apparatus used for the measurements is composed of a customized single-cylinder compression-ignition optical engine with engine speed controlled by a DC dynamometer. The engine is paired with a high-speed data acquisition system for engine cylinder-pressure measurements, a high-pressure common-rail fuel injection system, and an optical system designed to resolve the jet and combustion characteristics during and after the ROI ramp. The following is a description of the systems used experiments, as well as, a discussion of the post-processing algorithm used in analyzing the optical data.

3.1 Optical Engine

The engine block for the optical engine is a single cylinder engine block with balance shafts. A custom optically accessible cylinder head and piston were used for the current work. Schematic cross sections of the engine components used in the experiments are shown in Figure 1.

General mechanical specifications of the engine are summarized in Table 1. The cylinder head is an oil-less design that provides direct access to valvetrain components, has centrally located fuel injector access, and features overhead optical access that covers approximately 25% of the combustion chamber and extends to the wall to allow for jet-wall boundary analysis. For the current work, a stainless steel mirror optically polished to $<$20 Å was installed in head window location to allow for shadowgraphy to be simultaneously performed with Mie scattering measurements (process detailed below). The intake valve is shrouded, similar to the design in [50], which allows for control over the in-cylinder swirl ratio. The intake system for the engine provides control of in-cylinder density through control of the mass flow rate with a system of choked flow orifices of

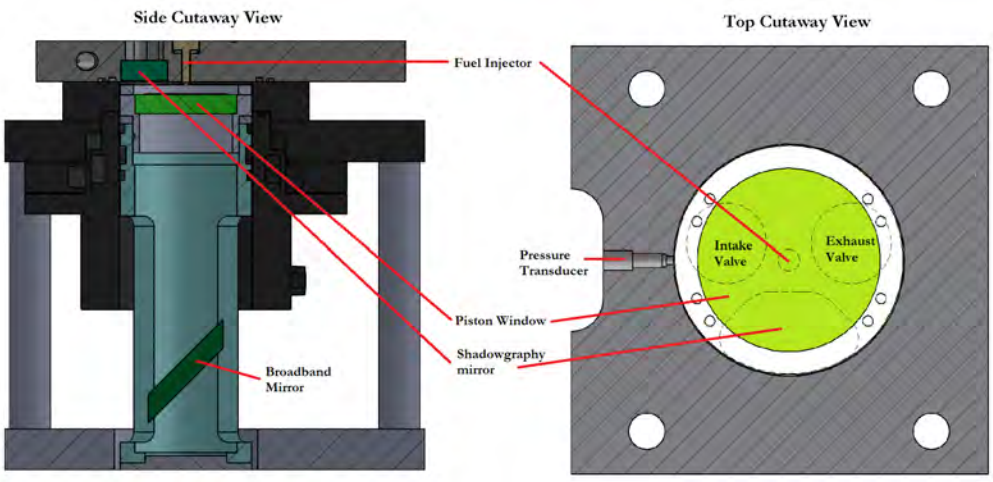

Figure 1: Schematic cross-section of the optical engine used in work-to-date.

Table 1: Engine Specifications

Parameter	Value
Engine type	Single-cylinder optical
Bore	82 [mm]
Stroke	76.2 [mm]
Piston optical access diameter	53.3 [mm]
Geometric compression ratio	14.03:1
Connecting rod length	144.8 [mm]
Swirl ratio range	0-5.5
Number of exhaust valves/intake valves	1/1
Cycle	4-stroke
EVO/IVO/EVC/IVC (degrees after compression TDC)	164/346/374/556 [CAD]

various sizes. Cylinder pressure is measured using a piezoelectric transducer (Kistler, 605BB60) sampled at 0.25 CAD resolution.

This engine utilizes the Bowditch extended piston design [51], which allows for optical access through a window in the piston. The piston crown holds a 29.0 mm thick UV grade fused silica window that provides a top-dead center (TDC) field-of-view of 53.3 mm. The piston bowl is a right cylinder, whose size was designed to allow for maximum length of jet penetration, while maintaining a sufficient compression ratio for compression ignition. Due to the proximity of the jet to the optical window surface, the engine had to be disassembled and cleaned after every three injections due to soot buildup on the piston window.

3.2 Fuel Injection System

The fuel injection system is composed of a second generation Bosch common-rail setup capable of stable injection pressures from 25-160 MPa. A Bosch CRIN 2 injector outfitted

with a custom, 6-hole injector tip from Stanadyne Inc. was used. With traditional common rail injectors, total flow area is one of the two methods of controlling the transient period of the injection, the other being the injection pressure. Increasing the total nozzle flow area or decreasing the injection pressure increases the ramp-up period. This type of injector operates by using the fuel injection pressure to overcome the force of a spring holding the tip needle closed. Higher fuel pressures open this spring faster, reducing transient period. To maximize the temporal resolution of the data over the transient period, a six-hole injector was used (as compared to similar tips that were available with only two or four tips), and injection pressure was a swept variable in the experiments to vary transient time.

The jet exits the injector at an angle of 13° out of the imaging plane, giving a maximum jet penetration distance along the spray axis of 29.4 mm before impinging upon the piston bowl. The hydro-ground orifices have diameters of 110 μm with k-factor = 1.5, representative of injectors used in small compression-ignition engines. Injections were controlled electronically, with injection timing determined from the optical encoder coupled to the engine crankshaft. The flow properties of the injector and the various tips have been characterized using a Bosch rate-of-injection meter [52] outfitted with a piezoelectric pressure transducer for rate-shape measurements [53]. The results comparing ROI of the maximum and minimum injection pressures during the initial transient portion of the rate shape are shown in Figure 2.

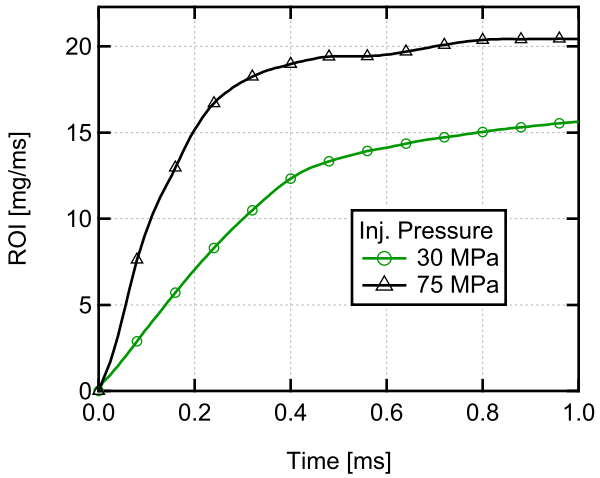

Figure 2: Rate-of-injection during the transient turn-on period for maximum and minimum injection pressures.

The dependence of the rate of increase of injection velocity on the injection pressure is visible in these plots. The range of injection pressures examined allows for durations of the initial injection transient of up to 500 μs.

Table 2: Engine Specifications

Property	Units	#2 diesel	JP-8 POSF 6169	HRJ
H/C ratio (mole based)		1.77	1.94	2.15
Net Heat of Combustion	MJ/kg	42.1	43.4	44.1
Cetane Number		46.1	44.8	57.4
Density (15°C)	g/cm^3	0.865	0.798	0.739
Viscosity (40°C)	cSt	2.71	1.30	0.75

3.3 Fuels and Engine Operating Conditions

Three primary fuels were used for the reported work. The first was an ultra-low sulfur #2 diesel fuel, chosen due to its prevalence in the literature and its ubiquity in modern compression ignition engines. A JP-8 fuel and a hydro-processed renewable jet fuel were chosen as the remaining test fuels due to their relevance for Army applications and to enable the influence of fuel properties to be investigated. The jet fuels have lower viscosities and densities than the diesel, as well as higher volatilities, as seen in Figure 3. The physical properties of the fuels are provided in Table 2.

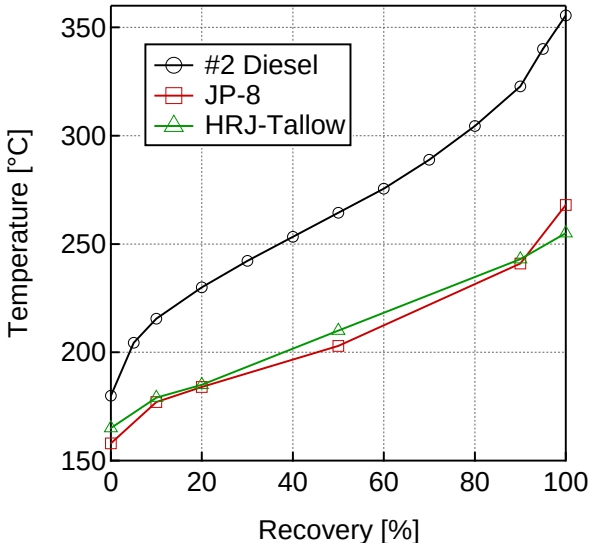

Figure 3: Distillation curves for #2 diesel fuel, JP-8 POSF 6169 and HRJ.

Each fuel was measured at the operating conditions given in Table 3. Measurements were performed at two in-cylinder densities and three in-cylinder temperatures. Three different injection pressures were tested at each density/temperature condition. This sweep of injection pressure provided a range of transient periods during the opening of the injector nozzle. Lower injection pressures result in longer ramp-up times, while increasing injection pressure results in ROI profiles approaching the square wave profile used in much of the literature. The in-cylinder swirl ratio was set to zero for all cases.

Table 3: Experimental Test Program

Property	Units	Value
In-Cylinder Density @ TDC	kg/m^3	15, 23
Fuel Injection Pressure	MPa	30, 52.5, 75
Injection Duration	μs	1500
SOI Timing	[CAD]	-5
Engine Speed	RPM	1200
Intake Air Temperature	°C	115, 125, 135

3.4 Optics and Imaging

The high-speed optical imaging system used for the work to date is capable of imaging the entire injection and combustion event while maintaining sufficiently high temporal resolution to resolve much of the initial fuel injection transient. The system was designed to provide simultaneous imaging of the vapor phase of the jet, the liquid phase, and the region of high-temperature combustion in the downstream portion of the jet in an internal combustion engine. In contrast, the majority of the relevant literature either images in a constant volume chamber or captures these processes separately, not simultaneously. The system layout is shown in two views in Figure 4.

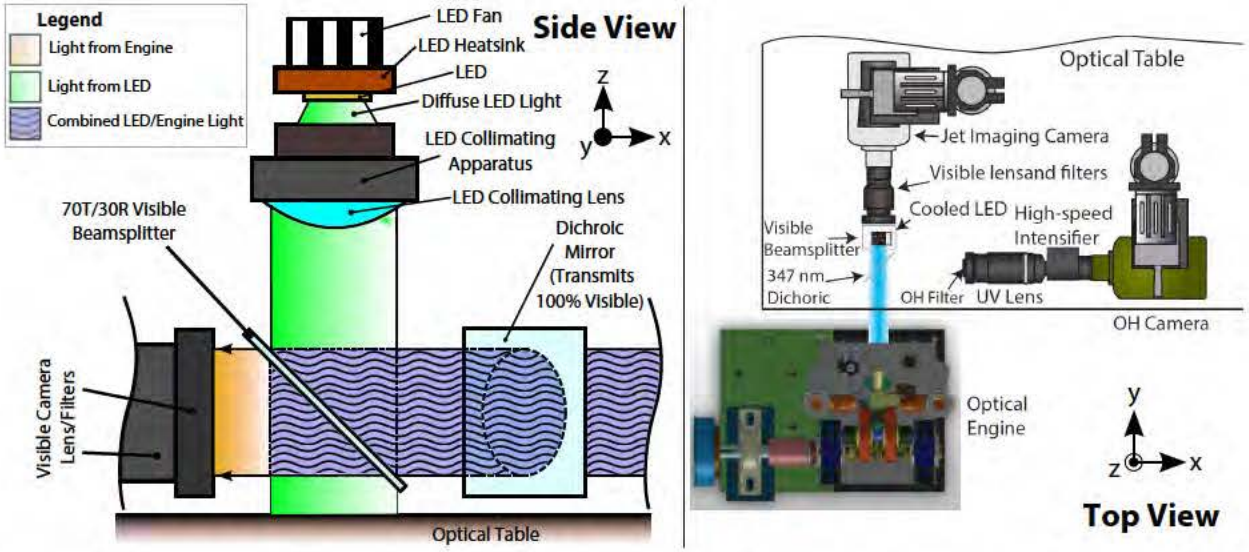

Figure 4: High-speed imaging system used for optical measurements of in-cylinder processes. Top view on the right, side view on the left.

Direction of light into and out of the engine is controlled by a pair of beamsplitters. A longpass dichroic beamsplitter (Semrock, FF347-Di01-50.4x71.2) reflects the ultraviolet hydroxyl radical (OH) chemiluminescence, an indicator of high temperature combustion and therefore the liftoff length, and transmits light in the visible spectrum including light from the LED used for shadowgraphy and Mie scattering illumination. A second, broadband beamsplitter (Edmund Optics, NT48-900) reflects 30% of the incident light and transmits 70% as seen on the left in Figure 4. The combustion chamber is illuminated

by a high power forced air-cooled LED (with maximum light output of 7.2 W) emitting light at a center wavelength at 462 nm (Luminus, CBT-120) that provides the lighting for jet visualization. A set of collimating optics are used to introduce the light emitted from the LED into the engine. The LED light that is immediately lost as it is reflected by the broadband visible beamsplitter is caught by an absorbing surface to prevent unnecessary reflections. Although the LED must be run at a higher power than would typically be required due to this initial 70% loss, it is not a limiting factor due to the high power capabilities of the LED system. The LED itself is a 1"x1" square circuit board with a small cooling system and remotely located power supply. A non-coherent light source such as an LED does not exhibit speckle [54] seen in more traditional laser-based setups.

The camera (Vision Research, Phantom v311) used for jet visualization is operated at a frame rate of 120.1 kHz with an exposure duration of 2.0 μs. The camera is outfitted with a F/1.4 85 mm focal length Nikkor lens. This frame rate provides for the capture of 60 frames within the initial 500 μs transient, allowing for resolution of the jet propagation and development for analysis while still maintaining a spatial resolution of 256 x 80 square pixels, at a pixel side size of 125 μm in the field-of-view. The low exposure duration reduces motion blur by limiting movement of the jet during a single frame, effectively freezing the flow motion over most of the field-of-view. A 60 nm bandpass filter centered at 460 nm is used to help reject much of the broadband soot incandescence and combustion luminosity while transmitting the LED light scattered back from the engine.

A second high-speed camera (Vision Research, Phantom v7.1) outfitted with a lens-coupled high-speed intensifier (Night-Vision Systems, S20 photocathode with P46 phosphor) is used for OH chemiluminescence imaging and liftoff length measurements. OH chemiluminescence centered in the UV at 310 nm is imaged onto the intensifier through a combination of a 280 nm longpass filter (Schott Glass, WG280) and a 80 nm FWHM bandpass filter centered at 300 nm (Semrock, FF01-300/80-25) fitted to a UV F/4.5 105 mm focal length Nikkor lens. The camera is operated at a frame rate of 40 kHz and an exposure duration of 20 μs. The longer exposure duration and slower frequency were required to obtain enough OH chemiluminescence signal for images of sufficient quality. Also, it is less necessary for extremely high (>100 kHz) frame rates in the region where this camera sees signals due to the downstream location of the lifted flame and concomitant lower local velocities. This method of imaging the location of high-temperature combustion via the chemiluminescence of the excited OH radical is well documented for use in optical engines [44, 55]. The vapor and liquid techniques used here are less conventional, and are explained briefly.

3.4.1 Vapor Imaging: Shadowgraphy

Imaging transparent gases such as fuel vapors requires special techniques such as Schlieren or shadowgraphy. As described in the scientific background, the index of refraction of a gas is a function of its chemical makeup, density, and temperature. Rays of light passing through regions that have gradients of these properties are steered, and can be focused into an image that has light and dark regions corresponding to the location of those gradients. The polished metal insert in the cylinder head allows for double-pass shadowgraphy to be used to detect vapor penetration. This surface promotes specular reflection of

the incoming LED light. As the incident and reflected light propagates through the fuel jet, gradients in density refract the light and change the amount of light returning to the camera, providing a clear indicator for the jet vapor penetration. A diagram illustrating the process via ray tracing is shown in Figure 5. This is a graphic representing the actual ray-tracing setup built in a CAD program that determines the quantitative effects of the presence of density and temperature gradients due to the refraction of the incoming LED light from the fuel vapor.

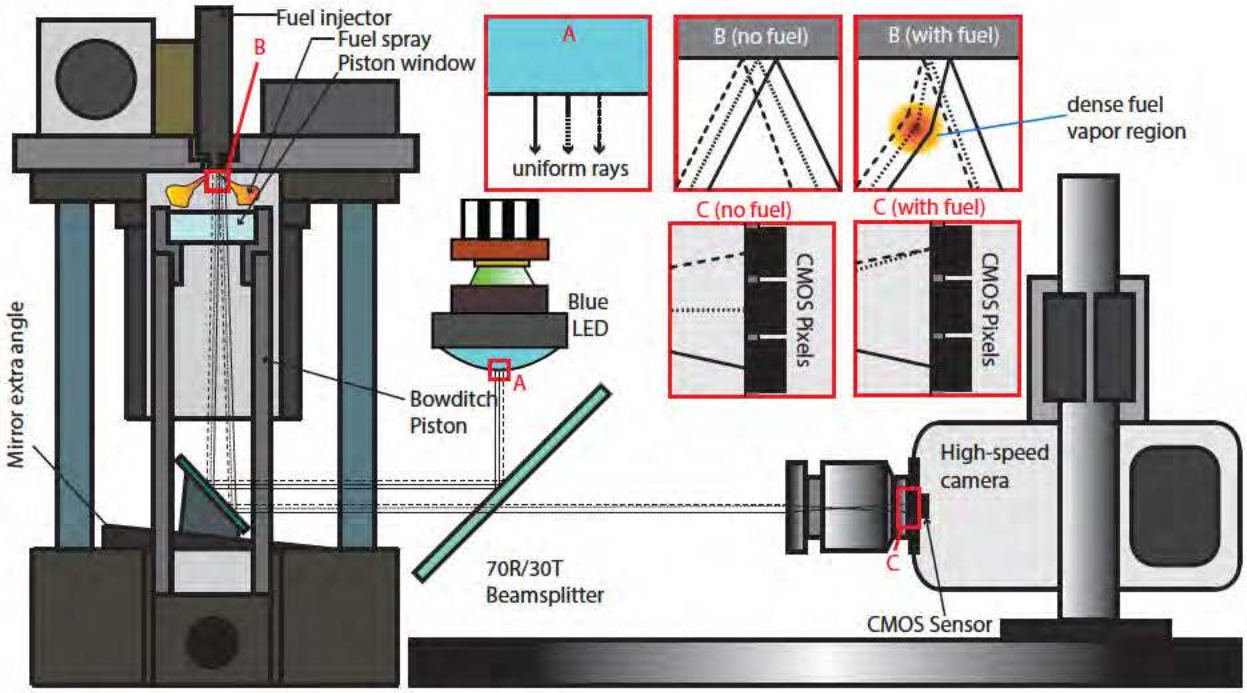

Figure 5: A ray-tracing diagram of the paths followed by the light imaged for shadowgraphy in vapor measurements.

The collimated LED light is introduced at angle of incidence of (1-5°) relative to the the head mirror, such that when no density gradients exist in-cylinder, the reflected light returns on a path that does not reach the camera sensor, and the image of the mirror appears dark. When the fuel jet passes in front of the mirror, providing gradients in density and temperature, the light rays are refracted to an angle closer to perpendicular with the mirror surface, and return along a path to the camera sensor. The term "double-pass shadowgraphy" comes from the fact that the beam is initially steered as it passes through the jet as it initially comes into the combustion chamber, and again after reflecting off of the mirrored surface. The error in position introduced from the short distance (< 5 mm) traveled between the jet and the mirror surface is negligible.

A similar setup for imaging liquid and vapor penetration was used in [56], although in that work the liquid and vapor diagnostics had to be imaged separately and chemiluminescence was not captured. Measurements involving fuel vapor usually involve Schlieren techniques which require direct optical access on a linear path into and then out of the apparatus, access which is possible with a CVC [5] but typically impossible in an engine

setting.

3.4.2 Liquid Imaging: Extinction

The liquid portion of the spray is composed of a dense region of very small droplets with size on the order of 10-20 μm [22]. It can be shown through Mie theory [57], given the index of refraction, number density, and droplet size, that these particles act as a diffuse surface. The extinction from forward scattering towards the head face prevents reflected light from returning to the camera, and the angle over which the droplets scatter the incoming light is large. Therefore, in the region where the vapor is also being detected, a strong gradient in signal is present where the liquid to vapor transition occurs. The rest of the cylinder head, which is more diffusely reflecting than the mirrored section, reflects much more of the incoming LED light directly back to the camera than scattering from the droplet cloud forming the liquid region. Scattering of the LED light by the dense liquid droplets attenuates the signal from its typical intensity associated with reflection off the cylinder head, reducing the number of photons returning to the camera in regions with liquid fuel. The amount of backscatter from the spray toward the camera is less than the level of attenuation caused by the spray, which results in an imaged signal with lower intensity than the surrounding background for the liquid regions in the spray.

3.5 Post-Processing Images

As discussed in the literature review, much of the recent jet measurement work uses single-pass Schlieren for vapor penetration and diffuse back illumination (DBI) for liquid penetration, techniques that require optical access from both sides of the experiment [58]. Light is provided from one side, passes through the jet, and is imaged on the other, a setup which is not practical in an optical engine when simultaneously measuring liquid and vapor penetration and liftoff length.

An effect from imaging light reflected from the head surface is that the background of the image is no longer uniform, which increases the complexity in distinguishing the jet intensity from the background. The majority of the literature works select an arbitrary pixel intensity threshold that best bound the visible jet [8], or choose a threshold centered between peaks in an intensity histogram [10], methods possible for images with constant backgrounds where the jet appears as a uniformly dark region against a bright background. These techniques are not sufficient for a non-constant background, as shown in part (a) of Figure 6, where the jet progresses over background gradients that range below and above the maximum intensity values of the jet.

Images taken from the high-speed camera are raster images, and are therefore easily converted to three-dimensional matrices with pixels ranging in count from 0 to 2^N, where N is the bit depth of the camera. An average background is then composed from a mean of the ten frames preceding the frame representing SOI and subtracted from all subsequent frames to be analyzed. The target frames then have a 3x3 median filter applied to them to reduce shot noise. The resultant image is shown in Figure 6 (b). The images are converted to polar coordinates, centered on the injector tip. This removes the need to

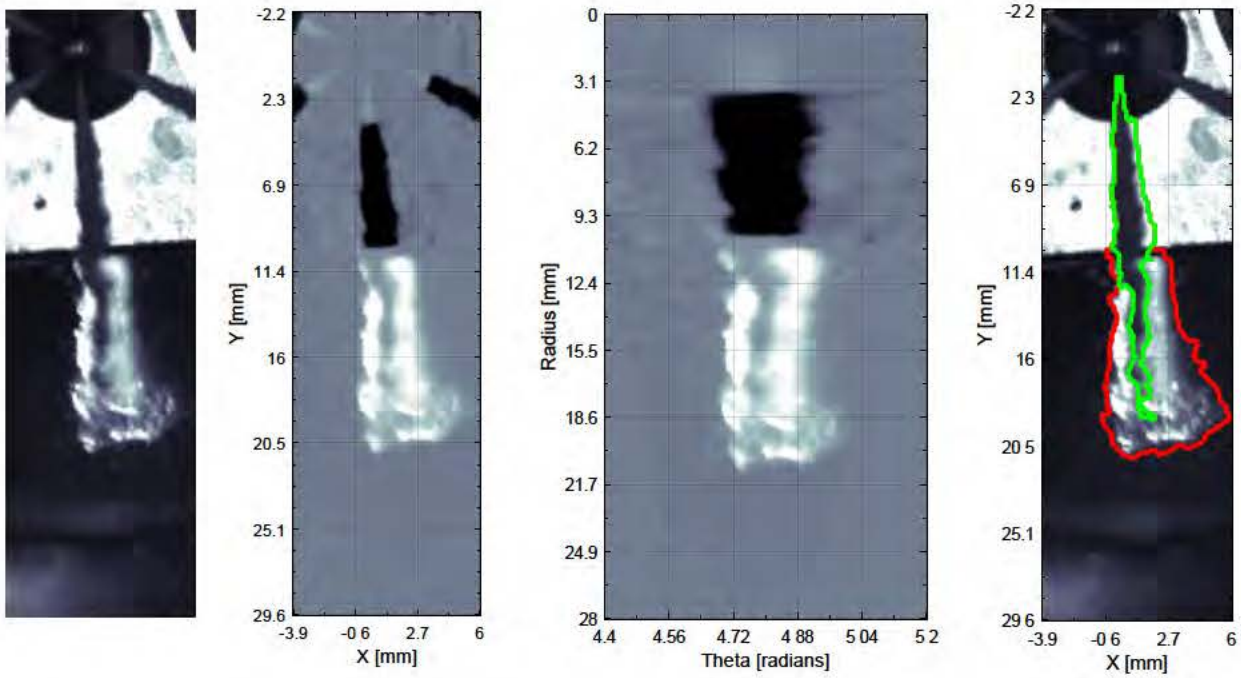

(a) (b) (c) (d)

Figure 6: Progressive images showing points in the post-processing performed on high-speed images of diesel fuel jets. Frames shown from (a) original video, (b) after subtracting background and applying median filter, (c) after converting to polar coordinates, and (d) converting results back to cartesian coordinates.

track the jet penetration along a non-Cartesian axis, and simplifies the dispersion angle measurements.

To account for gradients in the subtracted non-constant background that appear in the jet, a background weighted threshold matrix was used to discern between true background and true jet signal. First, a general threshold was chosen by applying Otsu's statistical method to the final background subtracted image, where the jet was fully developed. This method uses a closed-form solution to minimize the average error in assigning pixels to classes of average intensity. The algorithm maximizes between class variance by choosing optimum thresholds for each class. The effectiveness η of this method is calculated using Equation 7:

$$\eta(k_n^*, k_{n+1}^*) = \frac{\sigma_B^2(k_n^*, k_{n+1}^*)}{\sigma_G^2} \tag{7}$$

where σ_B is the between-class variance for class k, and σ_G is the variance of the entire image [59]. The number of classes was iteratively increased until the effectiveness η exceeded 99%. The general threshold was then set as the mean of the thresholds associated with the two lowest values of k, which represent the edges of the jet.

A matrix the size of the polar images was created, filled with this general threshold value, and then scaled over the radial axis r by the intensity distribution of the incoming power of the LED to compensate for non-uniform lighting. The polar version of the average background was then subtracted from this matrix, resulting in a threshold matrix whose level is chosen statistically, and sensitive to non-constant backgrounds and overall intensity non-uniformity. Edge refinement and noise rejection code is applied along with the threshold. This algorithm has performed flexibly over different lighting and background conditions without needing to tune constants or modify threshold levels. The liquid was distinguished from the vapor phase in a similar manner, by differentiating between the Otsu classes in the two-phase spatial range and only allowing low intensity classes enclosed by vapor to be classified as liquid.

The equation defining the spray angle, θ, is given by 8:

$$\theta = \tan^{-1}\left(\frac{A_{p,S/2}}{(S/2)^2}\right) \tag{8}$$

where $A_{p,S/2}$ is the projected spray area of the upstream half of the spray, and S is the penetration length. The penetration is defined as the distance along the spray axis where $1/2$ of the pixels on an arc of $\theta/2$ centered on the axis contain signal [10]. Determination of the regions of high-temperature combustion was accomplished using the Otsu statistical technique as well, although the videos corresponding to the OH chemiluminescence have a uniform background at the level of the dark noise of the camera, removing the need for a spatially weighted threshold.

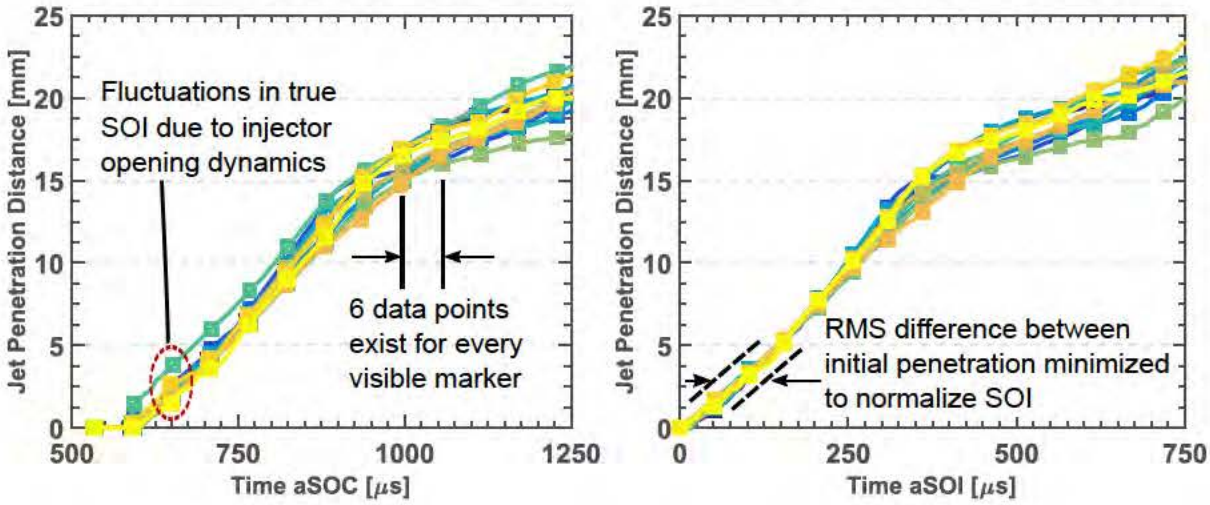

Figure 7: Process of aligning penetration data, adjusting for variance in SOC-SOI delay. Original, uncorrected data sets from post-processing algorithm in part (a), time-corrected sets in part (b).

3.6 Uncertainty Quantification and Ensemble Averaging

The uncertainty of single measured quantities and their uncertainties is represented by Equation 9:

$$X_i = X_{i,m} \pm \Delta X_i \quad (95\% \text{ confidence}). \tag{9}$$

The value of X_i is described by a measured value $X_{i,m}$ and an uncertainty ΔX_i so defined so as to have 95% confidence of X_i falling within the given range. Several sets of optical data were taken at each experimental condition, and there are multiple contributing sources of error in the optical measurements. Therefore, to define the uncertainty as introduced in Equation 9 for each of the quantities X_i as ΔX_i, another root-sum-square will be used to combine these effects [60]:

$$\Delta X_i = \sqrt{\Delta X_{i,1}^2 + \Delta X_{i,2}^2 + ... + \Delta X_{i,N}^2}. \tag{10}$$

In this case, ΔX_i represents the overall uncertainty for the given quantity, and $\Delta X_{i,1\rightarrow N}$ represent the individual uncertainty components making up the total uncertainty. In this work, two primary sources of uncertainty were identified; the case-to-case standard deviation in the measurements due to turbulence effects and small changes in experimental conditions, and uncertainty due to the experimental setup itself due to the limited time and spatial resolutions of the camera and optics setup. . The uncertainty interval to maintain 95% confidence for the mean (standard deviation, σ known) of a multi-sample experiment where the true mean is unknown requires interval estimation by assuming a normal distribution of the data about the true mean. Confidence intervals for many experiments can be calculated by calculating the Z-statistic, a value associated with the area under the normal distribution curve. For experiments with <120 samples, a t-statistic is calculated

for the area under the Student-t distribution, which is similar to the normal distribution, and allows for the estimation of the true mean by the sample mean. The measurements made in the data presented in this report involved 8-12 runs at each condition, so the t-statistic was used for confidence intervals [60, 61]. The equation for the t-statistic is given in Equation 11:

$$t = \frac{\overline{X} - \mu}{\frac{s}{\sqrt{n}}}. \tag{11}$$

Here, n is the sample size, s^2 is the sample variance (square of sample standard deviation), $\overline{X}$ is the sample mean, and μ is the population mean. The t-statistic is a known value as a function of % confidence, so the interval about a population mean for a given sample mean and standard deviation is calculated as:

$$\overline{X} \pm t_{n-1}\frac{s}{\sqrt{n}}. \tag{12}$$

The data presented in the results are primarily ensemble averages of multiple data sets. However, a small amount of fluctuation in the time between electronic start of injection command (SOC) and the actual SOI provided an incorrect penetration shape during averaging, as noted in [25]. To remove the uncertainty associated with variability in the exact SOI, the exact timing for the initial ramp-up of the penetration rates were shifted in time such that the root mean square error of the difference between the initial slopes of the ROI of each case was minimized, as seen in Figure 7. Data presented in the following section, unless otherwise specified, is the mean of N_m injection events where N_m ranges between 8 and 10.

4 Results

Jet penetration, liquid length, jet dispersion angle, liftoff length, and engine cylinder pressure data have been acquired over a range of compression-ignition engine operating conditions and fuel types. In this section, the general trends of these data over the range of conditions tested are first presented and compared to results seen in the literature. Next, behavior of these parameters is investigated during the initial transient development period of the jet as the length of the transient period is varied. Finally, the power law correlations of penetration with time and ambient density from the literature are compared to the correlations drawn to represent the transient data from the current work. The duration and shape of the unsteady portion of the ROI was a function of the injection pressure only. Plots of jet penetration, liquid penetration, and dispersion angle are bounded in time by SOI and the start of combustion. Liftoff length data begins when high-temperature signal was first detected, and ends when the mean liftoff length reached the injector orifice or too much signal existed in the image to correctly capture the correct length. For the jet parameters, data markers in plots are visible once for every five data points, and once for every three points in the liftoff plots.

4.1 Effects of Ambient Density, Injection Pressure, Intake Temperature, and Fuel Type on Jet Development

High-speed measurements of jet and combustion parameters were acquired for more than 50 different operating conditions encompassing variations in injection pressure, fuel type, intake temperature, and ambient cylinder density during the injection. The effects of these four parameters on liftoff length, jet penetration, liquid length, and dispersion angle are discussed, and example figures of the results are shown. Eight to ten runs were averaged for the data in each case presented in the data. Error bars in the plots represent the standard deviation about the mean of the samples taken, represented by markers. The shaded regions represent the 95% confidence interval bands for the mean of the data. Start of combustion times as found through analysis of the mean cylinder pressure traces are shown as vertical lines on the liftoff length plots and cylinder pressure/heat release plots. Methodology for finding the the start of combustion is taken from [62]. In direct-injection compression ignition engines, the injection of liquid fuel into the hot cylinder gases causes an evaporative cooling effect, resulting in a drop in cylinder pressure relative to an equivalent motored trace. The ignition delay is defined as the location where the fired cylinder pressure trace recovers its motored value due to combustion overcoming evaporative cooling.

4.1.1 Influence of Injection Pressure

The length and shape of the initial transient were controlled through the injection pressure, but this parameter has other effects on jet development as well. Three injection pressures were tested at each set of engine thermodynamic conditions and fuels. Time-resolved results for the selected case with $T_{intake} = 115^{\circ}$ C, $\rho_{amb} = 15$ kg/m^3 using diesel fuel are shown in Figure 8. The strong correlation between injection pressure and overall jet penetration is evident. As the fuel pressure increases, the increased liquid flow velocities at the injector orifice translate into higher penetration rates.

Conversely, changes in injection pressure have little effect on the quasi-steady liquid length, as the increase in injection velocity is offset by the increased air entrainment rate [28]. However, while the liquid lengths at each condition reach similar mean values, the variance in the data decreases with increased injection pressure. The fluctuations in liquid length were much larger for lower injection pressures. For the lower injection pressure cases, isolated regions of liquid would detach from the end of spray, causing a large sudden drop in the liquid length, a phenomenon less prevalent for higher fuel pressures. A sequence of images illustrating this effect is shown in Figure 10.

Although the final quasi-steady value of the dispersion angle for all three injection pressures was similar, the lowest injection pressure case also displayed a transient dispersion angle until the quasi-steady period of the rate-of-injection profile was reached, approximately 375 μs after the SOI. This increase in dispersion angle seems to correspond to a slight decrease in the liquid length. As the dispersion angle decreases to its final quasi-steady value the liquid length increases to its quasi-steady value. This effect decreased with increasing injection pressure, to a point where the dispersion of the jet at the highest injection pressure was nearly constant throughout the entire injection.

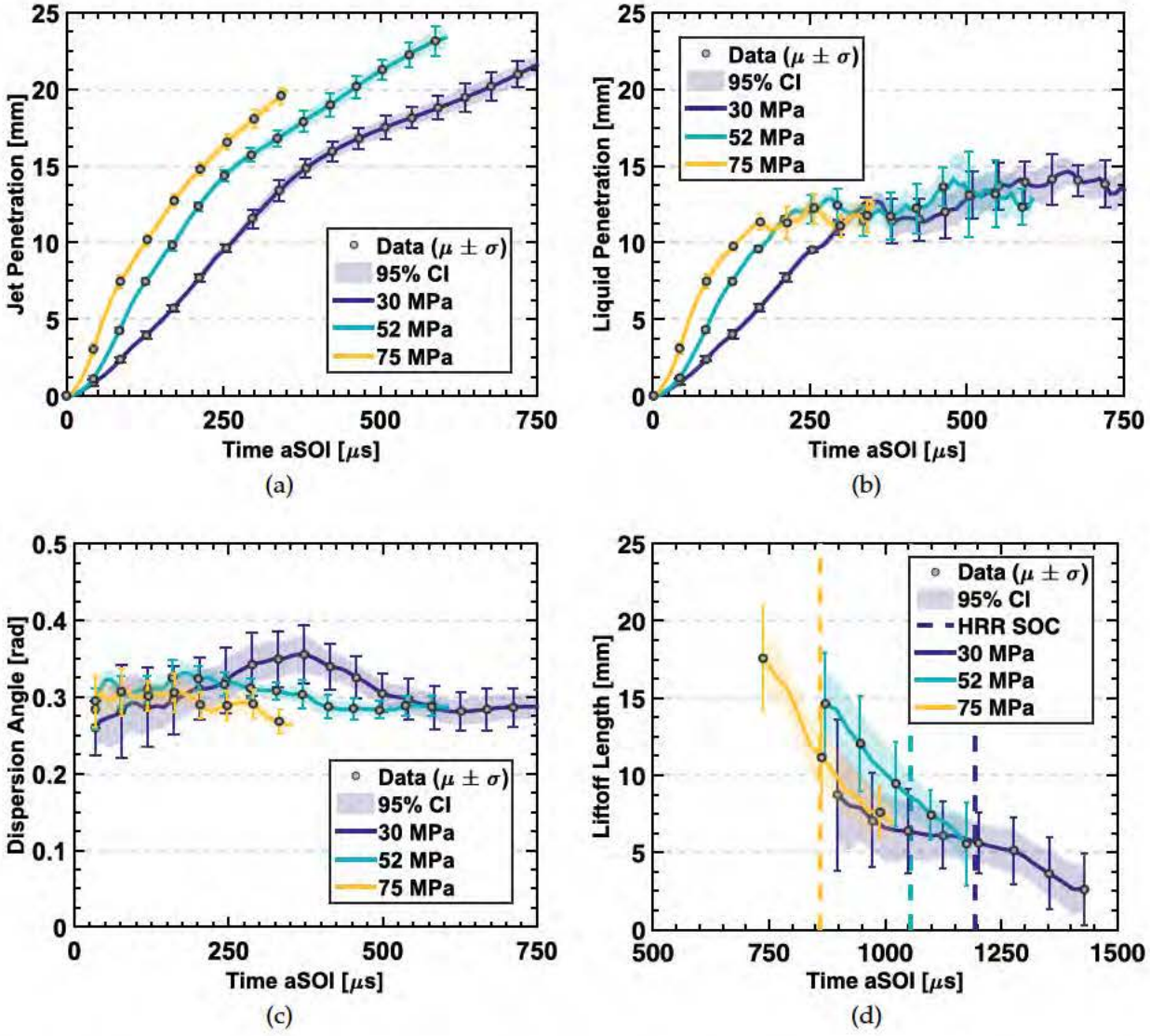

Figure 8: Optical results for a.) jet penetration, b.) liquid penetration, c.) dispersion angle, and d.) liftoff length against time for all injection pressures tested. Intake temperature of 115°C, in-cylinder density of 15 kg/m^3, diesel fuel.

The injection pressure has a strong influence on the ignition delay as illustrated by the earlier start of measurement for the liftoff length as injection pressure is increased. Higher injection pressures provided shorter ignition delays. These trends extend to the other thermodynamic cases measured as well. Although not as obvious as the influence of injection pressure on ignition delay, the initial liftoff length following ignition is generally increased with higher injection pressure. Following ignition, the liftoff length for all injection pressures rapidly decreases due to compressive heating of the in-cylinder ambient gases. The ignition delays determined from the cylinder pressure measurements are consistently 2 CAD (278 μs) longer than the delay between SOI and chemiluminescence initially appearing in the images. The chemiluminescence first observed around the time

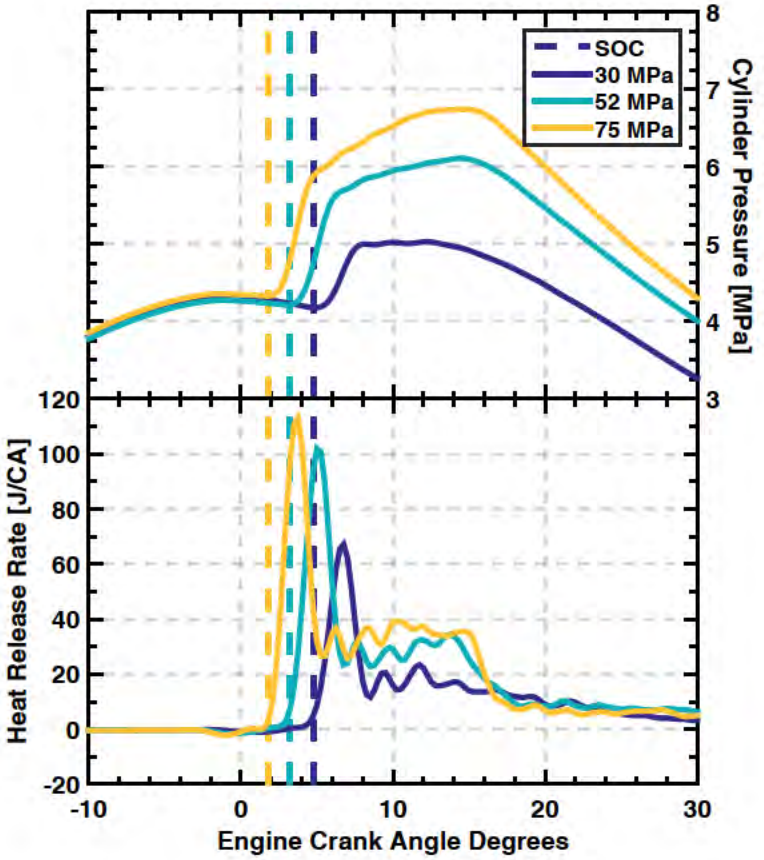

Figure 9: Engine cylinder pressure and heat release rates for all injection pressures tested. Intake temperature of 115°C, in-cylinder density of 15 kg/m^3, diesel fuel.

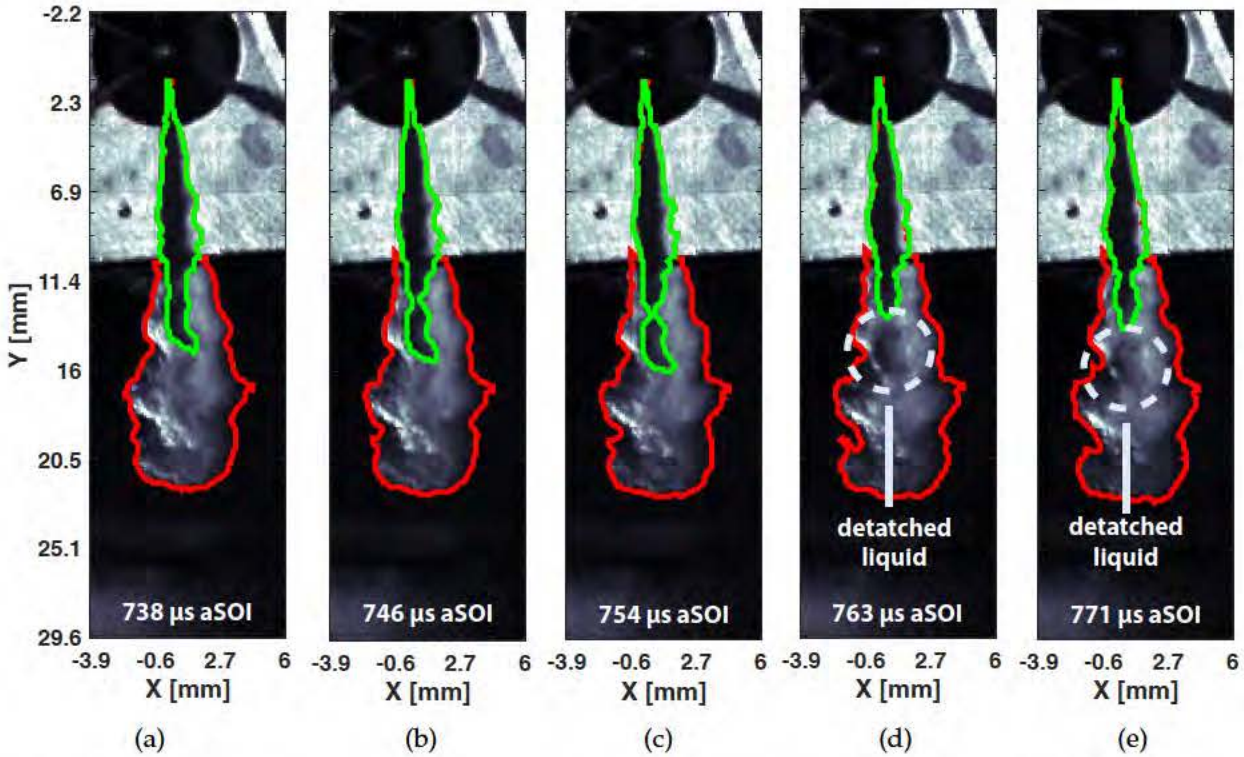

Figure 10: Sequence of images showing the progression of the liquid length and subsequent detachment of a liquid segment. In the images, the vapor boundary is outlined in red whereas the boundary between liquid and vapor is outlined in green.

of ignition starts as small kernels that grow with time into a larger region. These small kernels are trackable optically and associated with the liftoff length, but it is not until sufficient heat release has occurred in-cylinder to overcome the pressure decrease due to evaporative cooling that the ignition delay is determined from the in-cylinder pressure measurement. This results in the observed delay between the chemiluminescence based determination of ignition delay and that determined from the in-cylinder measured pressure.

4.1.2 Influence of Intake Air Temperature

Jet and combustion parameters for the case with $\rho_{amb} = 15$ kg/m^3 and $P_{inj} = 30$ MPa using diesel fuel are presented in Figure 11. As was expected, the jet penetration was not affected significantly by changes in intake temperature when the ambient density is held constant. The liquid lengths were also not significantly affected by this change. Although temperature is a key factor in the vaporization rate of the fuel jet, the range of temperatures swept for the intake conditions was not large enough to strongly affect the liquid length during injection.

This range of temperatures at engine intake were also not wide enough to strongly affect the liftoff lengths. Liftoff length in general showed much larger standard deviation

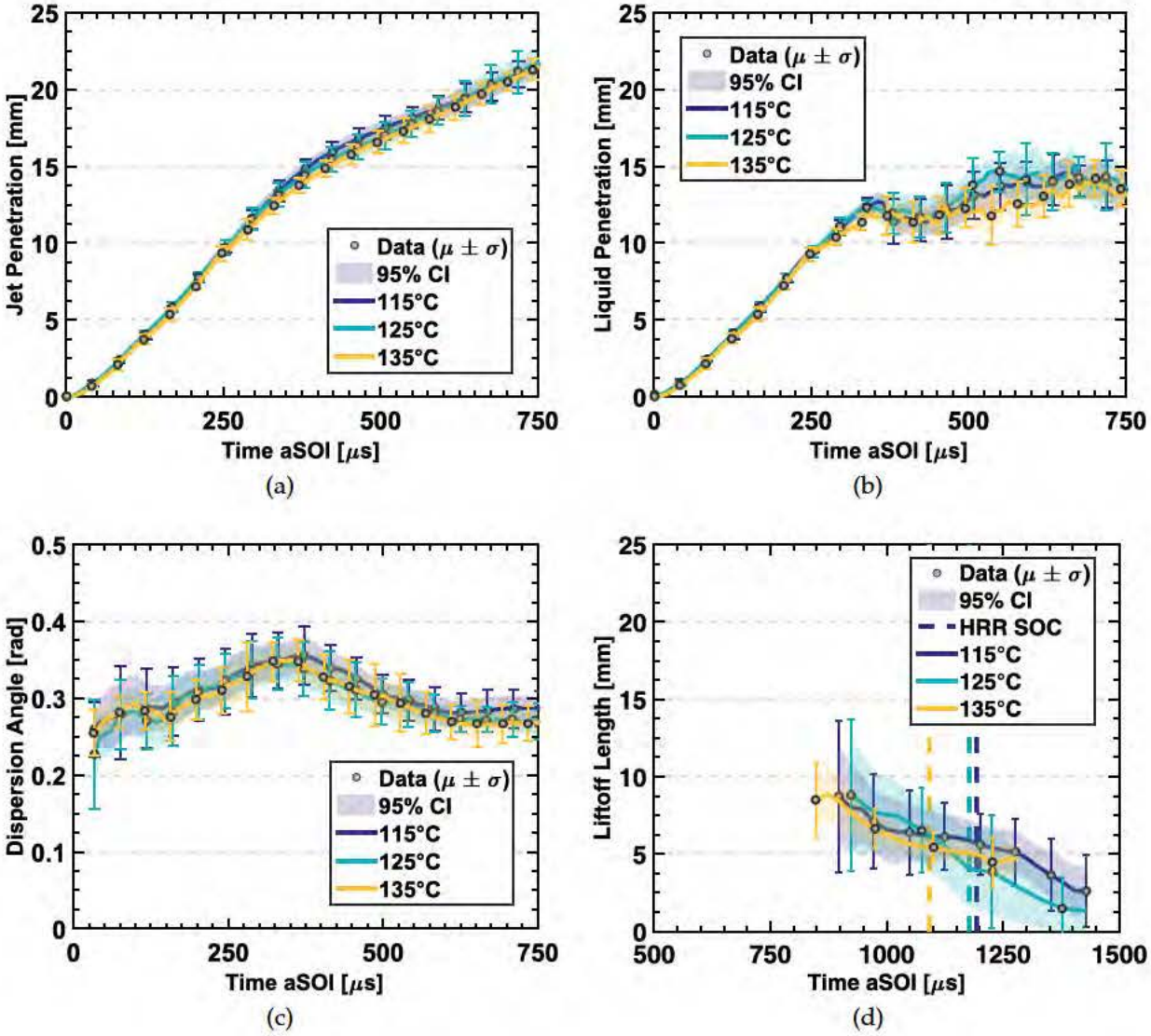

Figure 11: Optical results for a.) jet penetration, b.) liquid penetration, c.) dispersion angle, and d.) liftoff length against time for all intake temperatures tested. Injection pressure of 30 MPa, in-cylinder density of 15 kg/m^3, diesel fuel.

than the other parameters measured. This variance was evident in both the location and time of the initial ignition kernel.

4.1.3 Influence of In-Cylinder Density

Measurements were taken for two in-cylinder ambient densities specified at TDC, which occurred halfway through the duration of the injection. In-cylinder thermodynamic conditions in an reciprocating engine vary with time due to piston motion. However, the piston speed near TDC is relatively slow and the injection event lasts 10 CAD, from -5 to +5 degrees TDC, causing a small but finite density change of 3-4% over the injection

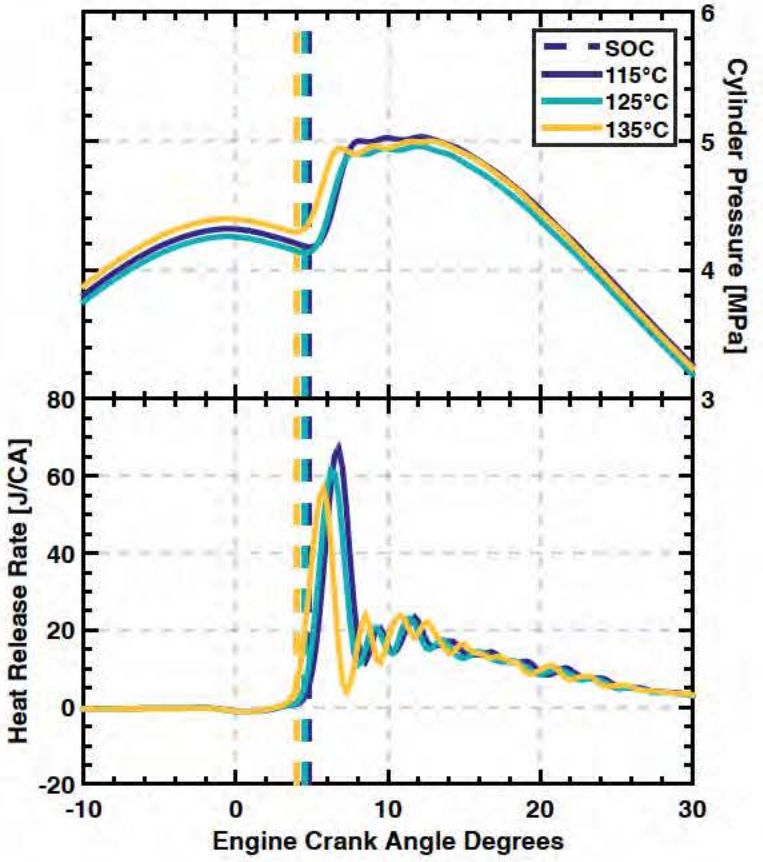

Figure 12: Engine cylinder pressure and heat release rates for all intake temperatures tested. Injection pressure of 30 MPa, in-cylinder density of 15 kg/m^3, diesel fuel.

event for all tested cases.

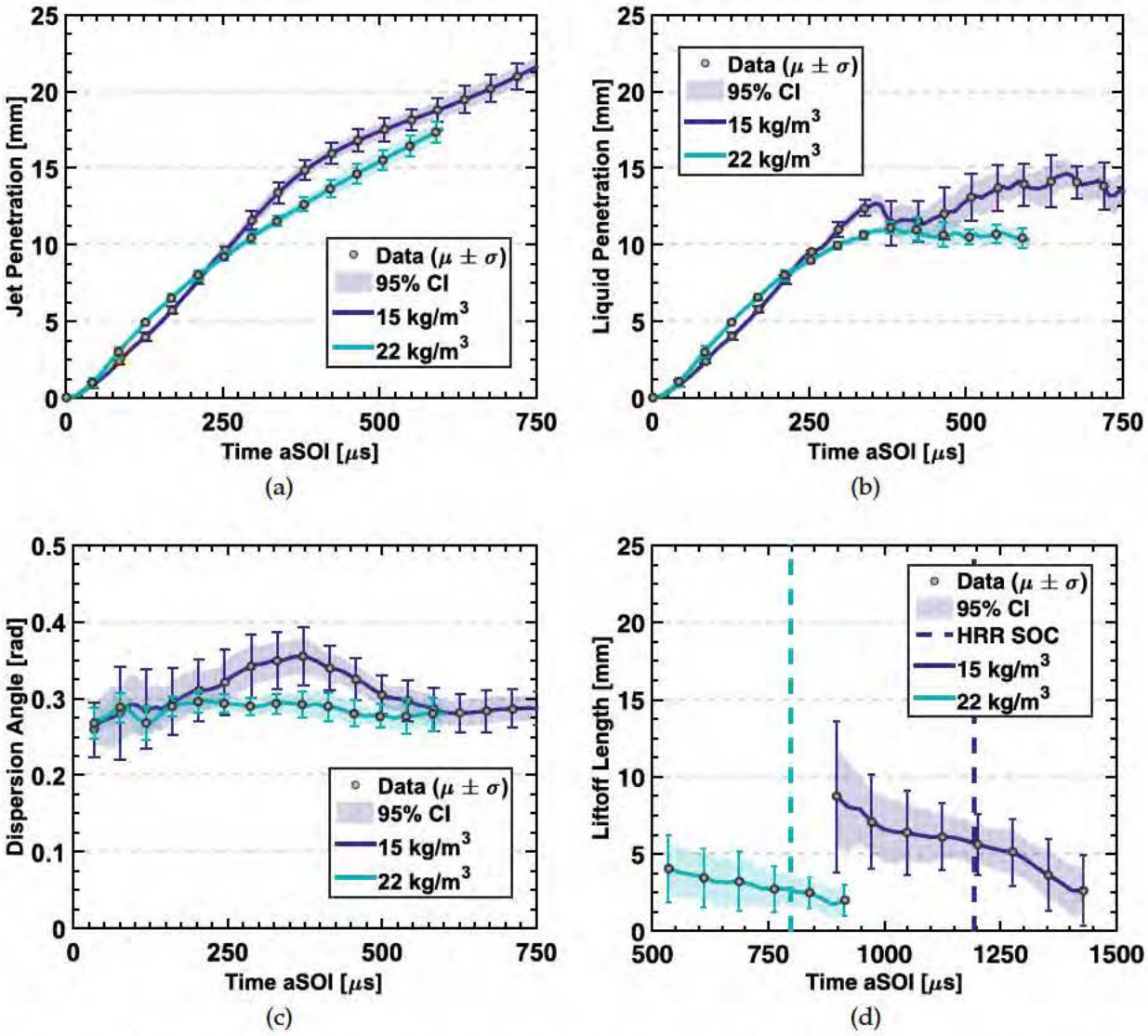

Figure 13: Optical results for a.) jet penetration, b.) liquid penetration, c.) dispersion angle, and d.) liftoff length against time for all in-cylinder densities tested, and diesel fuel. Intake temperature of 115°C, injection pressure of 30 MPa.

Ambient density was seen to reduce the quasi-steady values of liquid length and vapor penetration length, as seen in the case using diesel fuel with an intake temperature of 115°C, and injection pressure of 30 MPa shown in Figure 13. This is as expected, jet penetration and liquid length scale inversely in a non-linear manner with ambient density in the long time limit [11, 28]. For short times, the jet penetration was slightly larger for higher ambient density cases, as seen in Figures 13 and 14. This effect was greater for diesel fuel, and should be explored further. The dispersion angle did not show any statistically significant trends with density once the quasi-steady injection period was reached.

Liftoff lengths were strongly affected by changes in ambient density. The overall mean

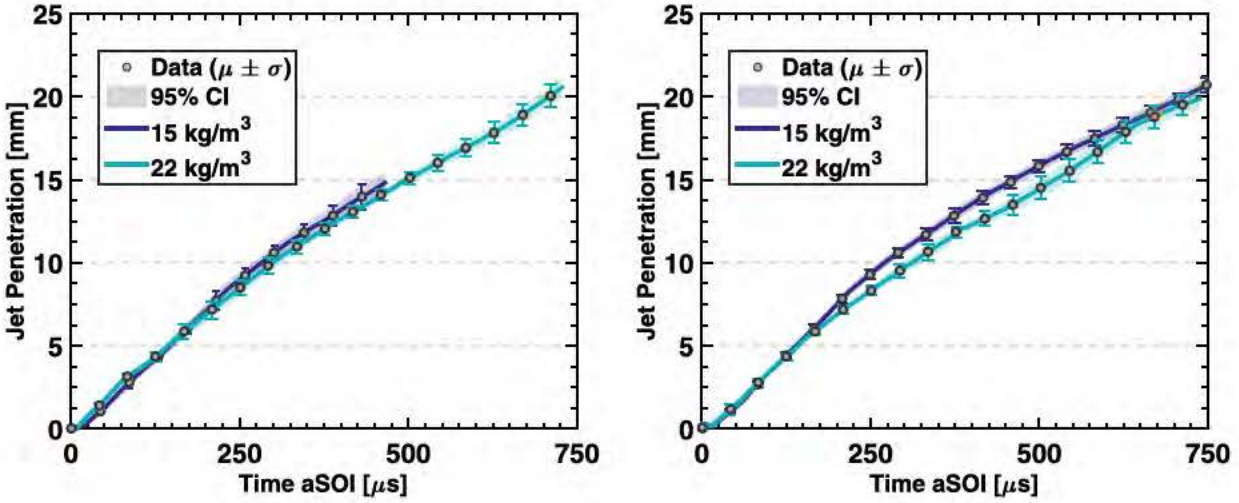

(a) (b)

Figure 14: Additonal jet penetration results over all densities for a.) JP8 and b.) HRJ. Intake temperature of 115°C, injection pressure of 30 MPa.

liftoff length decreased with increasing density, and the ignition delay was severely reduced with the increase in ambient density. Increasing ambient density enhances jet mixing, resulting in faster energy transfer from hot cylinder gases to the fuel.

4.1.4 Influence of Fuel Type

The jet fuels had higher volatility than the #2 diesel fuel, decreasing the distance and time required for the liquid fuel to evaporate completely. This is reflected in data for case $\rho_{amb} = 15$ kg/m^3 and $P_{inj} = 30$ MPa in Figure 16. The jet fuels displayed shorter jet penetration and liquid lengths than the diesel test fuel due to the volatility differences between the fuels.

The combustion results did not follow the same trend. The diesel and JP8 fuels developed similar liftoff and ignition delay profiles, while the HRJ fuel ignited earlier and maintained a liftoff distance closer to the injection orifice. As shown in Table 2, HRJ has a significantly higher cetane number than the other two fuels indicating it should have the shortest ignition delay, a result seen in Figure 17. The #2 diesel fuel and the JP8 fuel used have cetane numbers that are the same within the reproducibility limits of the cetane number test. The matched liftoff length history and ignition delays for the JP8 and #2 diesel fuel agree with previous observations that the volatility difference between the fuels does not significant impact ignition delay and combustion if cetane number is matched between the fuels [62, 63]. The results are reflected in the ensemble averaged engine cylinder pressure results and associated heat release results presented in Figure 17. The heat release and cylinder pressure results confirm the similarity of the combustion process for the #2 diesel and JP8 fuels. It is evident from the heat release that for all fuels, a large percentage of the fuel is combusted in the initial premixed burn, with a relatively small fraction of heat release associated with the mixing controlled combustion at these low

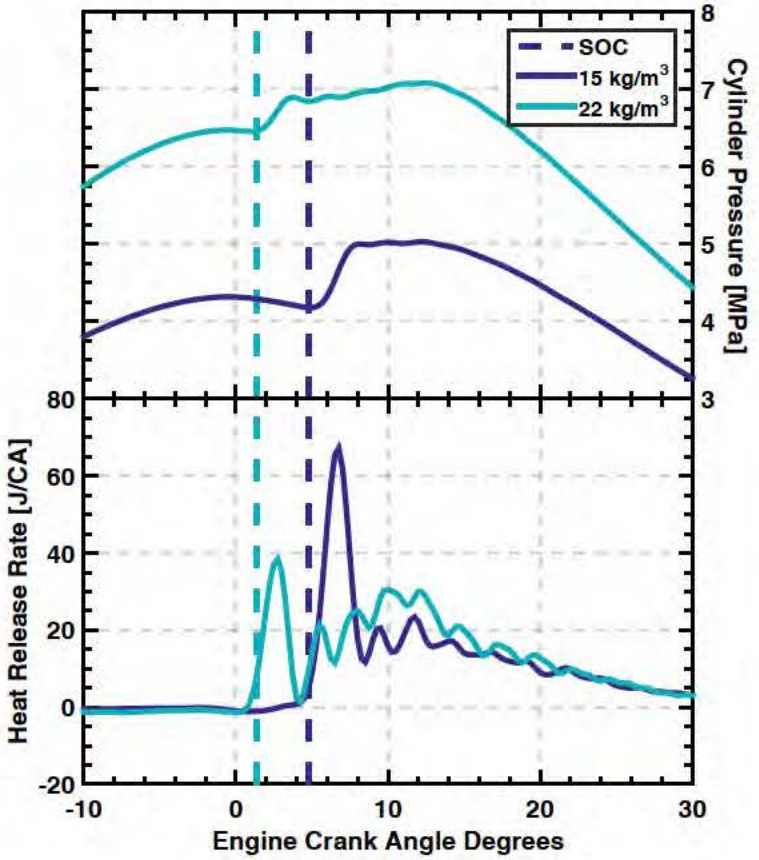

Figure 15: Engine cylinder pressure and heat release rates for all in-cylinder densities tested. Intake temperature of 115°C, injection pressure of 30 MPa, diesel fuel.

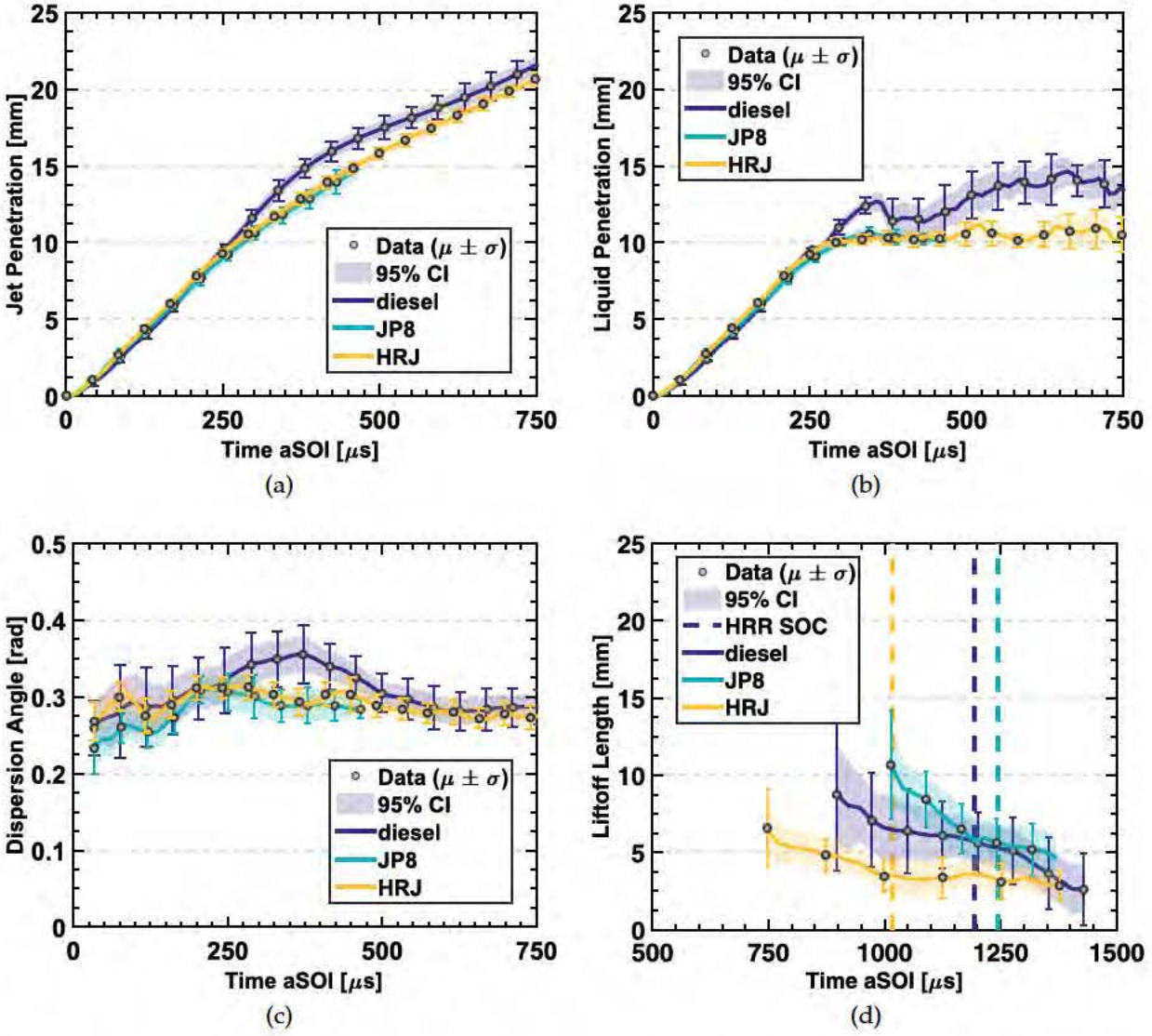

Figure 16: Optical results for a.) jet penetration, b.) liquid penetration, c.) dispersion angle, and d.) liftoff length against time for all fuels tested. Intake temperature of 115°C, injection pressure of 30 MPa, in-cylinder density of 15 kg/m^3.

density conditions where the ignition delay is long.

4.2 Impact of Initial Transient ROI on Jet Development

It was shown in the previous section that in an optically accessible internal combustion engine , during the quasi-steady portion of the injection process the jet and combustion parameters measured agreed with general trends from similar experiments in constant volume chambers [10, 28]. The following section explores deviations from quasi-steady behavior when the injection velocity is not constant during the initial ramp-up of the injection process.

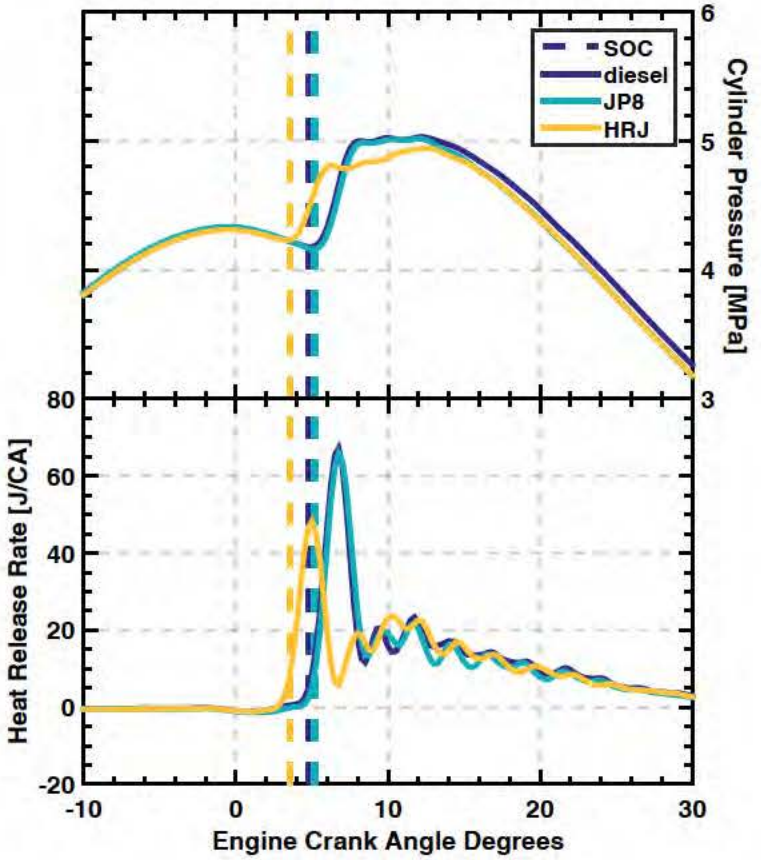

Figure 17: Engine cylinder pressure and heat release rates for all fuels tested. Intake temperature of 115°C, injection pressure of 30 MPa, in-cylinder density of 15 kg/m^3.

4.2.1 Jet Behavior During Transient ROI

The transient part of the injection event is due to a varying fuel flow rate as the injector needle lifts from covering the injector orifices. As the fuel pressure overcomes the spring force holding the injector shut, the flow area increases to its maximum value over a non-negligible time duration, and the mass flow rate changes from initially zero to a quasi-steady value. This rise in mass flow rate affects the penetration rate of the jet during its initial development when it is dominated by the momentum of the liquid spray. The penetration relationship proposed by Hiroyasu [11] predicts a linear scaling of penetration with time until t_{break}, then a $t^{1/2}$ scaling afterwards. For this work, the best fit for the scaling of jet penetration with time was found. Similar to previous work, a power law equation of the form:

$$S(t) = \beta t^a \tag{13}$$

was found to fit the data well, where β is a empirical constant and a is the power law exponent. Three values of a and β were found for each condition tested, one pair fit to the initial (short time) data points, one to the transition period of the jet, and the other fit from data in the quasi-steady (long-time) regime. The jet penetration data initially presented in Figure 8 is shown on a log-log scale, overlaid with the curve fits given by Equation 13, is in Figure 18. The values of a derived to best fit the data are also included in the plot.

Three linear segments present themselves in jet penetration on a log-log scale, separated by clear inflection points. Similar to previous results in the literature, the dependence on time, a, for the long-time limits were all close to a $t^{1/2}$ scaling. However, in the period before the jet transitions from its ramp-up state while the opening transient is present, the experimental results deviate from the literature. Equation 1 predicts a linear relationship with time during this period, but the fits derived from the data displayed a nonlinear scaling with time. This results was seen for measurements at all conditions tested. The t^1 dependence from the literature assumes a constant mass flow velocity, and during the liquid-momentum dominant phase, the penetration velocity would also be constant. The acceleration in mass flow rate due to the opening of the injector tip, however, increases this dependence to be >1, as seen in Figure 18.

It is clear that S is strongly affected by the opening of the injector during the initial development stage, but transitions to conventional quasi-steady behavior afterwards. Therefore, although the initial ROI transient affects the jet penetration while the transient is occurring, the head of the jet eventually transitions to the time dependence predicted in the literature [11]. Although quasi-steady dependence of penetration on time is achieved for long injection durations, a significant error will still exist due to the difference at early times.

4.2.2 Jet Velocity and Unsteady ROI During the Injection Transient

In order to directly compare the effect of the rate of fuel injection on jet penetration, the velocity of the jet tip, $\frac{dS}{dt}$, is presented with the time rate of change of mass flow, $\frac{dROI}{dt}$, in Figure 19. The derivative of the curve fit defined in Equation 13 is defined by the following

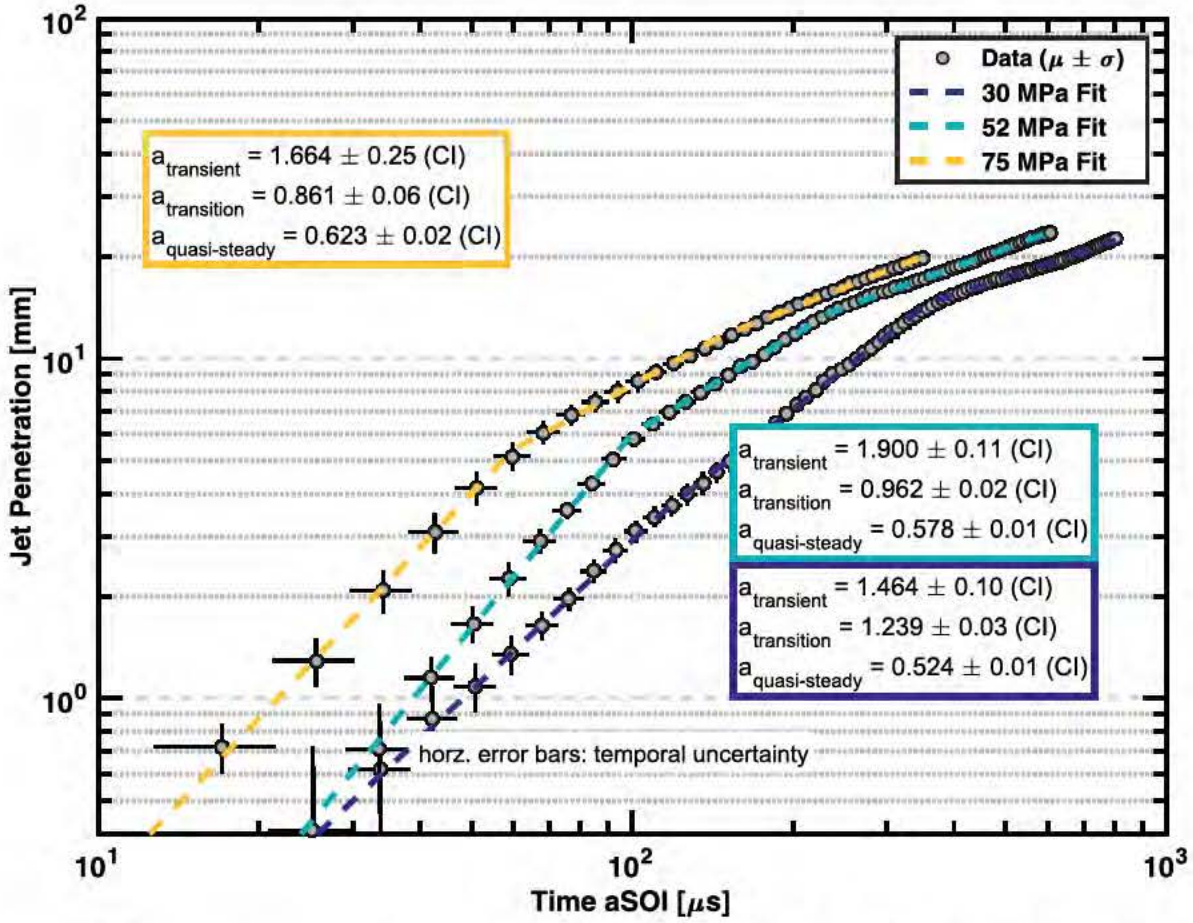

Figure 18: Jet penetration on a log-log scale, with curve fits of the form in Equation 13 included. Diesel fuel at an intake temperature of 115°C, and in-cylinder density of 15 kg/m^3.

equation:

$$\frac{dS}{dt} = a\beta t^{a-1}. \tag{14}$$

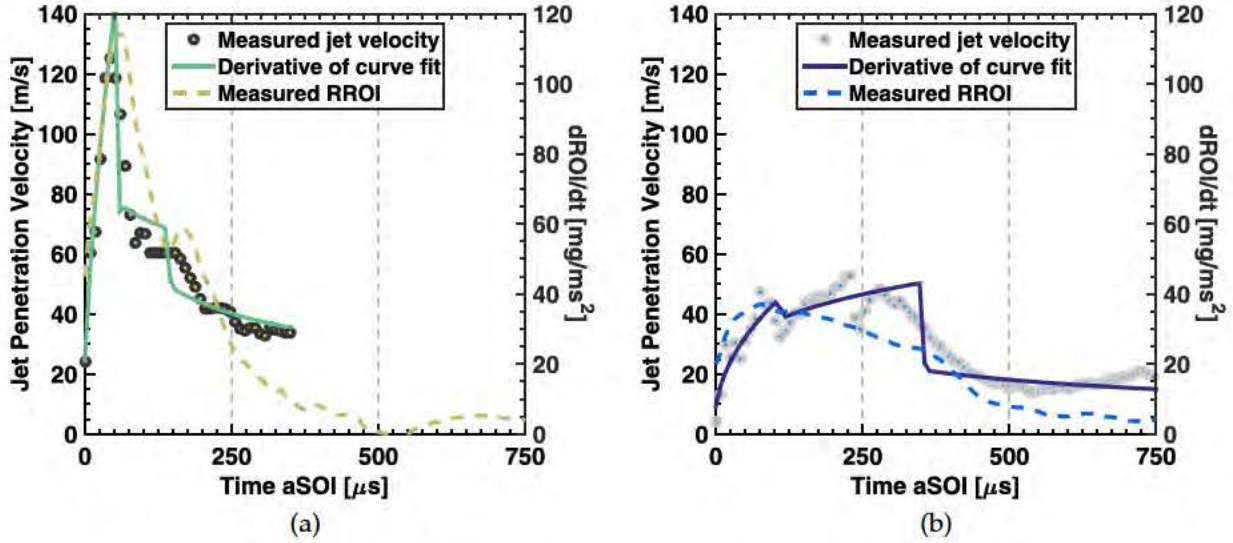

Figure 19: Comparison of the jet penetration velocity, rate of ROI, and the derivative of the curve fit from Equation 13. Conditions of ρ_{amb}=15 kg/m^3, T_{intake}=115°C, using diesel fuel.

The jet penetration velocity as predicted by Equation 14 correctly represents the boundary condition of $\frac{dS}{dt} \rightarrow 0$ for $t \rightarrow 0$. This is in contrast with the non-physical constant spray tip velocity down to t=0 implied from the derivative of Equation 1, an issue noted in [25]. Excluding the period of transition where the penetration shifted from its short to long time behavior, the derivative of the curve fit describes the behavior of the actual spray tip velocity reasonably well.

The shape of $\frac{dROI}{dt}$ also appears to follow a similar trend as the time dependence of the jet velocity during the transient period. The correlation between ROI and tip penetration velocity falls off as the jet reaches its long-time behavior. This relationship between the derivative of the ROI and the jet tip penetration velocity provides an possible method of approximating jet penetration for cases with injection transients. Rather than assuming a constant mass flow rate, the actual time dependence of the ROI of the injector could be measured and possible relations between initial ROI and penetration developed. Injector ROI is a much easier quantity to experimentally measure than actual optical jet data.

4.2.3 Transient ROI Effects on Liftoff Length and Combustion

The experimental conditions run were such that the delay between SOI and initial combustion were relatively long compared to the time between SOI and the shift of the jet to its quasi-steady region. Therefore, by the time high-temperature reactions began, the jet

was no longer experiencing the effects of the initial transient. The main effect the non-constant ROI has on the combustion of jets under these conditions is the change in fuel mass injected. If the injection event truly followed an instant-on profile, the mass injected would be greater, resulting in a change in engine load.

Transients of this form, then, exert secondary effects on the successive combustion event. For instance, the transient injection will alter the rate of air entrainment and, therefore, the subsequent ignition delay and initially established liftoff length. Again, the actual effect the transient has on combustion is increased as the injection duration decreases. For cases where the injection ends before it reaches its quasi-steady state, the effects of the transient on fuel mass and mixing will more directly affect the ignition location and liftoff length.

5 Summary and Impact

As mentioned in the results, in the environment of an internal combustion engine, the quasi-steady regions of the jet and combustion parameters measured agreed with general trends seen in scaling predictions from constant volume chambers in the literature. This indicates that with the correct tuning parameters, the relationships developed between the testing conditions and the resulting jet features for chambers can be applied in engine work as well. However, it is now evident that this is true only for cases where the the injection is dominated by its quasi-steady region. This happens when either the the transient time is short relative to the steady portion, or if the injection follows an instant-on, "top-hat" style of ramp-on. The error caused by deviations from these scaling laws increases as the ratio of transient to non-transient portions increases.

The primary results and conclusions based on the findings from the current study are:

- High-speed measurements of jet parameters and compression ignition combustion were obtained simultaneously in an optical engine whose specifications are similar to those of modern commercial small-bore diesel engines. This was achieved by designing and implementing a front-illuminated optical setup that used Mie scattering for liquid length determination and dispersion angle measurements, double-pass shadowgraphy for vapor measurements, and chemiluminescence for determination of liftoff length. The jet measurements were obtained at a frame rate of 121 kHz so as to capture in detail the penetration during the entire injection, with key interest in the initial ramp-up transient seen in hydraulically-activated fuel injectors.

- High-pressure fuel jets in internal combustion engines were found to follow the same trends with ambient and injection conditions as results taken previously in constant volume chambers. Key observations include reduction in jet and liquid penetration with ambient density, increase in jet penetration with injection pressure, and decrease in quasi-steady liquid length with fuel volatility.

- The influence of fuel properties on the jet parameters was also characterized using two jet fuels. The higher volatility and lower density of the jet fuels relative to #2 diesel fuel resulted in shorter liquid lengths for the jet fuels and slight differences in

the jet dispersion and penetration. However, the lift-off length and ignition delay for the JP8 fuel were almost identical to the #2 diesel fuel with matched cetane number, indicating that cetane number has a stronger influence than changes in fuel physical properties on the combustion process.

- The effects of the injector opening process were studied by varying the injection pressure, which modified the fuel mass rate-of-injection from initially zero to a quasi-steady value. Analysis of the jet penetration results revealed three distinct scalings with time, as opposed to the two-regime methodology used in the literature. The jet was seen to initially have a scaling with time of t^a, with $a > 1$, moving to a stage where the scaling was approximately linear, and eventually transitioning to the $t^{1/2}$ scaling expected for these types of jets in the long-time domain [11]. The initial time scaling varied with injection pressure, and the transition to $t^{1/2}$ scaling with time indicates the point at which the transient has ended, and the jet is following the scaling predicted for long times from the literature [11].

- The penetration velocity of the jet was compared to the derivative of the ROI, or the rate of change of mass flow from the injector. For the cases considered, these parameters followed similar scaling with time. This suggests that the ROI of a jet, which is experimentally much easier to measure than actual optical penetration data, could possibly inform transient effects on the scaling of jet parameters with time, although further work is needed to confirm this theory.

The transients introduced by the injector opening process influenced the jet tip penetration velocity for the duration of the opening process. Jet development then transitioned to behavior expected of a quasi-steady process after the injector was fully open. Therefore, injections whose quasi-steady portion is long relative to the transient period can be well described by the scaling relationships from the literature, while short injections dominated primarily by the opening and closing periods of the injector cannot assume an instant-on injection profile, and must take the rate of injection scaling with time into consideration to correctly model jet behavior.

References

[1] Stone, R. *Introduction to Internal Combustion Engines*. Society of Automotive Engineers, Warrendale, PA, (1999).

[2] Higgins, B., Siebers, D., and Aradi, A. *SAE Technical Paper* **2001-01-0940** (2000).

[3] Heywood, J. *Internal combustion engine fundamentals*. McGraw-Hill, New York, (1988).

[4] Dec, J. *SAE Technical Paper* **970873** (1997).

[5] Pickett, L. M., J., M., Genzale, C. L., Siebers, D. L., Musculus, M. P. B., and Idicheria, C. A. *SAE Technical Paper* **2011-01-0686** (2011).

[6] Som, S., D'Errico, G., Longman, D., and Lucchini, T. *SAE Technical Paper* **2012-01-1263** (2012). 2012-01-1263.

[7] Pickett, L. M., Genzale, C. L., Bruneaux, G., Malbec, L., Hermant, L., Christiansen, C., and Schramm, J. *SAE Technical Paper* **2010-01-2106** (2010).

[8] Pickett, L. M., Manin, J., Payri, R., Bardi, M., and Gimeno, J. *SAE Technical Paper* **2013-24-0001** (2013).

[9] Hay, N. and Jones, P. *SAE Technical Paper* **720776** (1972).

[10] Naber, J. D. and Siebers, D. L. *SAE TRANSACTIONS* **105**(3), 82–111 (1996).

[11] Hiroyasu, H. and Arai, M. *SAE Technical Paper* **900475** (1990).

[12] Varde, K. S. and Popa, D. M. *SAE Technical Paper* **830448** (1983).

[13] Reitz, R. D. and Bracco, F. B. *SAE Technical Paper* **790494** (1979).

[14] WU, K. J., Steinberger, R. L., Santavicca, D. A., Bracco, F. V., and Su, C. C. *Journal of Fluids Engineering* **105**(4), 406–413 (1983).

[15] Payri, F., Payri, R., Bardi, M., and Carreres, M. *Experimental Thermal and Fluid Science* **53**(0), 236 – 243 (2014).

[16] Zhang, Q. and Johari, H. *Physics of Fluids (1994-present)* **8**(8), 2185–2195 (1996).

[17] Johari, H. and Paduano, R. *Experiments in Fluids* **23**(4), 272–280 (1997).

[18] Breidenthal, R. E. *Physica Scripta* **2008**(T132), 014001 (2008).

[19] Abani, N. and Reitz, R. D. *Physics of Fluids (1994-present)* **19**(12), – (2007).

[20] Silva, C., Neto, P., and Pereira, J. *Theoretical and Computational Fluid Dynamics* **23**(4), 287 – 296 (2009).

[21] Payri, R., Salvador, F. J., Gimeno, J., and de la Morena, J. *SAE Int. J. Engines* **1**, 528–536 04 (2008).

[22] Wakuri, Y., Fujii, M., Amitani, T., and Tsuneya, R. *Bulletin of JSME* **3**(9), 123–130 (1960).

[23] Dent, J. C. *SAE Technical Paper* **610002** (1961).

[24] Abraham, J. *Numerical Heat Transfer Part a-Applications* **30**(4), 347–364 (1996).

[25] Kostas, J., Honnery, D., and Soria, J. *Fuel* **88**(11), 2225 – 2237 (2009).

[26] MUSCULUS, M. P. B. *Journal of Fluid Mechanics* **638**, 117–140 Nov 10 (2009).

[27] Musculus, M. P. B. and Kattke, K. *SAE Technical Paper* **2009-01-1355** (2009).

[28] Siebers, D. L. *SAE Technical Paper* **980809** (1998).

[29] Espey, C. and Dec, J. E. *SAE Technical Paper* **952456** (1995).

[30] Siebers, D. L. *SAE Technical Paper* **1999-01-0528** (1999).

[31] Kamimoto, T., Yokota, H., and Kobayashi, H. *SAE Technical Paper* **871610** (1987).

[32] Canaan, R. E., Dec, J. E., Green, R. M., and Daly, D. T. *SAE Technical Paper* **980510** (1998).

[33] Higgins, B. S., Mueller, C. J., and Siebers, D. L. *SAE Technical Paper* **1999-01-0519** (1999).

[34] Fisher, B. and Mueller, C. *SAE Int. J. Engines* **5**(2), 415–429 (2012). 2012-01-0463.

[35] Fisher, B. T. and Mueller, C. J. *Fuel* **89**(10), 2673 – 2696 (2010).

[36] Fisher, B. T., Knothe, G., and Mueller, C. J. *Energy and Fuels* **24**(9), 5163–5180 (2010).

[37] Dec, J. and Coy, E. B. *SAE Technical Paper* **960831** (1996).

[38] Pickett, L. M. and Siebers, D. L. *International Journal of Engine Research* **7**(2), 103–130 (2006).

[39] Gaydon, A. *The Spectroscopy of Flames*. Chapman and Hall Ltd., (2000).

[40] Peters, N. *Turbulent Combustion*. Cambridge University Press, (2000).

[41] Siebers, D. L. and Higgins, B. *SAE Technical Paper* (2001). 2001-01-0530.

[42] Pickett, L. M., Siebers, D. L., and Idicheria, C. A. *SAE Transactions* **114**(3), 1714 (2005).

[43] Pauls, C., Grnefeld, G., Vogel, S., and Peters, N. *SAE Technical Paper* **2007-01-0020** (2007). 2007-01-0020.

[44] Donkerbroek, A., Boot, M., Luijten, C., Dam, N., and ter Meulen, J. *Combustion and Flame* **158**(3), 525 – 538 (2011).

[45] Wu, Y., Huang, R., Liu, Y., Leick, M., and Lee, C.-f. F. *SAE Technical Paper* **2010-01-0606** (2010).

[46] Pickett, L. M. and Siebers, D. L. *International Journal of Engine Research* **7**(2), 103–130 (2006).

[47] Juneja, H., Ra, Y., and Reitz, R. D. *SAE Technical Paper* **2004-01-0530** (2004).

[48] Settles, G. S. *Schlieren and shadowgraph techniques : visualizing phenomena in transparent media*. Springer, Berlin New York, (2001).

[49] Mcnaught, A. D. and Wilkinson, A. *IUPAC Compendium of Chemical Terminology, 2nd ed.* Wiley-Blackwell, (1997).

[50] Heim, D. and Ghandhi, J. *SAE Int. J. Engines* **4**(1), 1642–1668 (2011). 2011-01-1287.

[51] Bowditch, F. W. *SAE Technical Paper* **610002** (1961).

[52] Bosch, W. *SAE Technical Paper* **660749** (1966).

[53] Bower, G. R. and Foster, D. E. *SAE Technical Paper* **910724** (1991).

[54] Pickett, L. M., Kook, S., and Williams, T. C. *SAE Int. J. Engines* **2**(1), 439–459 (2009). 2009-01-0658.

[55] Musculus, M. P. B. *SAE Technical Paper* **2003-01-0074** (2003). 2003-01-0074.

[56] Pastor, J. V., Payri, R., GARCIA-OLIVER, J. M., and Briceno, F. J. *Atomization and Sprays* **21**(6), 503–520 (2011).

[57] Hulst, H. v. d. *Light Scattering by Small Particles*. Dover Publications, Inc, New York, (1987).

[58] Manin, J., Bardi, M., and Pickett, L. M. *Proceedings of the 8th International Conference on Modeling and Diagnostics for Advanced Engine Systems, COMODIA 2012* , 665–673 (2012).

[59] Gonzalez, R. *Digital image processing*. Prentice Hall, Upper Saddle River, N.J, (2008).

[60] Moffat, R. J. *Experimental Thermal and Fluid Science* **1**(1), 3 – 17 (1988).

[61] Levine, David M., P. P. R. and Smidt., R. K. *Statistics for Engineers and Scientists: Using Microsoft Excel and MINITAB*. Prentice Hall, (2001).

[62] Rothamer, D. A. and Murphy, L. *Proceedings of the Combustion Institute* **34**(2), 3021 – 3029 (2013).

[63] Pickett, L. M. and Hoogterp, L. *SAE Technical Paper* **2008-01-1083** (2008).